Chemical Geology 514 (2019) 10–26

Contents lists available at ScienceDirect

Chemical Geology

journal homepage: www.elsevier.com/locate/chemgeo

Element mobility and spatial zonation associated with the Archean Hamlet orogenic Au deposit, Western Australia: Implications for fluid pathways in shear zones

Shawn B. Hood[a,b,*], Matthew J. Cracknell[a,b], Michael F. Gazley[d,e], Anya M. Reading[b,c]

[a] Centre for Ore Deposit and Earth Sciences (CODES), University of Tasmania, Hobart, Tasmania, Australia
[b] ARC Industrial Transformation Research Hub for Transforming the Mining Value Chain (TMVC) at CODES, Hobart, Tasmania, Australia
[c] School of Natural Sciences (Math and Physics), University of Tasmania, Hobart, Tasmania, Australia
[d] RSC Mining and Mineral Exploration, 93 The Terrace, Wellington, New Zealand
[e] Victoria University of Wellington, PO Box 600, Wellington, New Zealand

ARTICLE INFO

Editor: Karen Johannesson

Keywords:
Mass balance
Metasomatism
Ore deposit
Orogenic gold
Shear zone
Fluid flow
Archean
St Ives
Hamlet
Au lode

ABSTRACT

Mass balance equations can be used to understand metasomatism. Here we use 2726 multi-element chemical analyses to quantify the effect of metasomatism associated with Au mineralisation at the Hamlet Gold Mine (Hamlet), Yilgarn Craton, Western Australia. Principal components analysis is first used to identify covarying elements and six groups of elements are identified: (1) relatively immobile elements, with Zr and Hf providing an appropriate reference frame for mass balance calculations; (2) elements associated with mafic rocks, such as Ca, Co, Fe, Ge, Mg, Mn, and Zn; (3) elements related to potassic alteration, Ba, Cs, K, Rb, and Tl; (4) elements related to sodic alteration, Be, Na, and Sr; (5) chalcophile elements, including Bi, weakly associated with Au; and (6) Au, Te, and S representing the main Au-mineralising event. A statistically-rigorous approach is then used to quantify element addition and depletion and provides 95% confidence limits for changes in mass. To achieve this, the basaltic host rocks are divided into four subunits based on Cr content. Sample subsets are then created to select altered rocks and least-altered protolith rocks, using discrimination diagrams. Pairings of least altered-altered samples from each basalt subunit are used to construct matrices via bootstrapping. Mass balance results from these matrices indicate similar element mobility associated with Au mineralisation across the four basalt subunits, with up to 24% mass loss. Key potassic and sodic group elements are enriched in the Au mineralised zones at the expense of elements with a mafic-association. Spatial patterns of mass change are linear and repetitive within the steeply-dipping Hamlet Shear Zone, interpreted to represent a mesh-like geometry of metasomatism within the plane of the shear zone. Localised enrichment of K, Na, and Bi are related to Au distribution while Ca depletion zones reflect the movement of reactive fluid along the shear plane.

1. Introduction

Orogenic Au deposits can provide a sample-rich opportunity to investigate geochemical changes associated with deformation-focussed metasomatic activity. While univariate geochemical data or element ratios can be an effective first-pass method to investigate chemical distribution and relative abundance for a region (Reimann, 2005), these approaches do not quantify element addition or depletion. Methods to quantify geochemical changes include: (1) calculating 'enrichment factors' using ratios, where the element concentration of interest is divided by the concentration of an immobile element (Chandrajith et al., 2001; Brauhart et al., 2017; Carranza, 2017); (2) Pearce Element Ratios (Stanley and Madeisky, 1996; Whitbread and McQueen, 2002; Urqueta et al., 2009); and (3) calculating mass balance, where the ratio of immobile element concentration for an altered and unaltered (or least-altered) sample provide a reference frame for computing element addition or loss (Gresens, 1967; Grant, 1986, 2005; McKinley et al., 2016).

Geochemical mass change in open-systems has been discussed extensively in the literature (Gresens, 1967; Grant, 1986; Brimhall and Dietrich, 1987; Brimhall et al., 1988; Ague and van Haren, 1996). An application of mass balance calculations is to quantify element changes in metasomatically-altered rock, relative to the unaltered (or least-altered) rock representing the protolith. The results provide information

* Corresponding author at: Centre for Ore Deposit and Earth Sciences (CODES), University of Tasmania, Hobart, Tasmania, Australia.
E-mail address: Shawn.Hood@utas.edu.au (S.B. Hood).

https://doi.org/10.1016/j.chemgeo.2019.03.022
Received 4 December 2018; Received in revised form 14 March 2019; Accepted 20 March 2019
Available online 27 March 2019

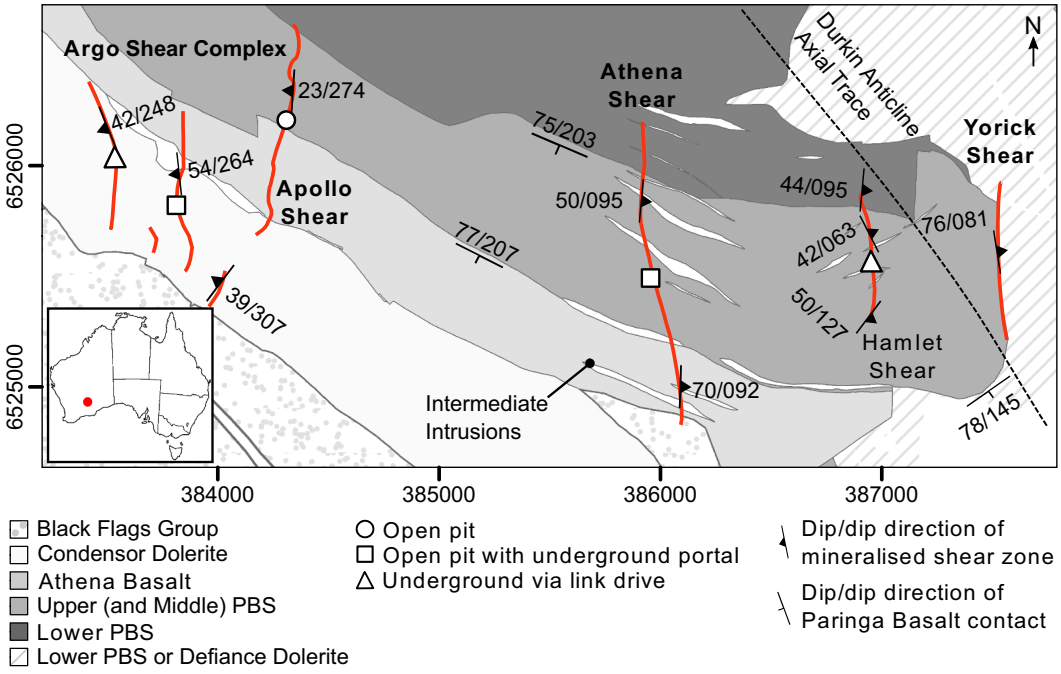

Fig. 1. Bedrock map of St Ives, Western Australia, showing the Paringa Basalt (PBS) and mineralised shear zones (red) within the greater Argo-Athena-Hamlet shear complex. The axial trace of the Durkin Anticline is shown as a dashed line. Map drafted using unpublished company mapping and the drill data used in this study. (For interpretation of the references to colour in this figure legend, the reader is referred to the web version of this article.)

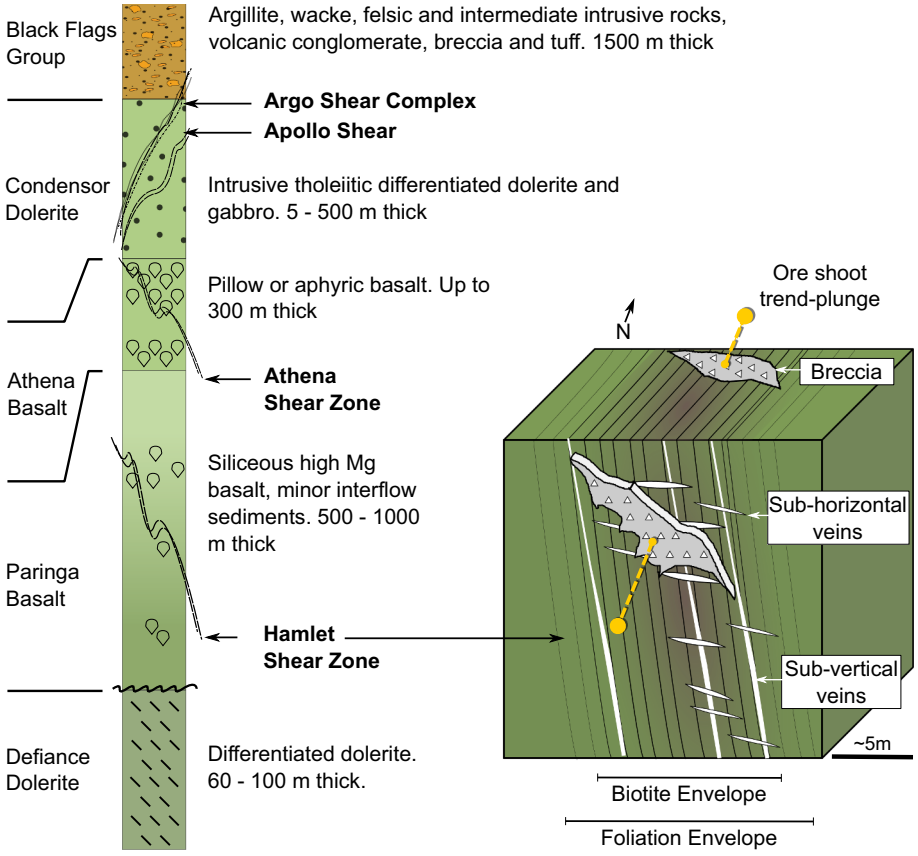

Fig. 2. The stratigraphic column on the left shows the relative location of the Paringa Basalt and mineralised shear zones shown in Fig. 1. A schematic representation of the Hamlet Shear Zone with hallmark features is shown on the right. Stratigraphic descriptions and thicknesses are from McGoldrick et al. (2013a) and Gregory et al. (2016).

about the effects of overprinting metasomatism experienced by the altered rock or suite of altered rocks. In this study, a statistically-robust elemental mass balance investigation is presented for the Hamlet Gold Mine (Hamlet; Fig. 1). The methodology provides a technique to model hydrothermal fluid flow pathways in three dimensions (3-D), and results improve our understanding of element mobility in shear-associated greenstone Au (orogenic Au) deposits. To support mass balance results, Principal Components Analysis (PCA; Pearson, 1901; Jolliffe,

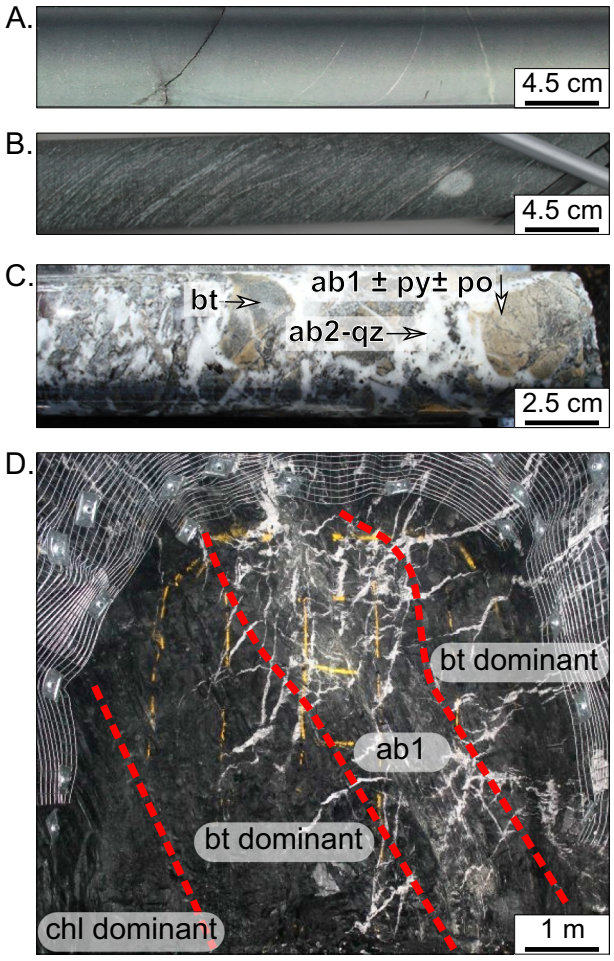

Fig. 3. Mineralogical zones of Paringa Basalt related to the Hamlet Shear Zone which represent ore-distal to ore-proximal facies. A. Drill core sample of massive chlorite-bearing basalt from outside the shear zone. B. Drill core showing schistose altered rocks, characterised by biotite replacement of chlorite. Sample is from within the shear zone. C. Drill core sample of brecciated brown albite (ab1) and biotite (bt) altered rock with disseminated pyrrhotite (po) and lesser pyrite (py). The breccia matrix is white albite (ab1) and qz. D. Underground mining face (8805 Ore Drive North) showing the relationship between rocks from figures A—C, separated by red dashed lines. Gold mineralised rocks with pervasive ab1 alteration are central to the Hamlet orebody. This zone is flanked by more weakly mineralised, biotite-altered rocks without ab1. These two facies overprint greenschist-metamorphosed basalt.

2011) is used to produce groups of elements associated with protolith rock composition or overprinting alteration effects.

2. Geochemical mass balance

The conventional graphical mass balance approach of Grant (1986, 2005) is not well-suited to highly-variable rock composition, noisy data and/or large datasets. First, the immobile element reference frame selected can strongly affect the outcome of mass change estimates. This is because major and trace element concentrations differ by orders of magnitude. Very-low concentrations near the analytical detection limit contribute less to the position of the isocon than higher values, analytical errors, and the variable mobility of “immobile elements” (e.g., Baumgartner and Olsen, 1995; Mukherjee and Gupta, 2008; Ahmed et al., 2019). Second, parent protolith rocks are chemically heterogeneous and altered rocks are not uniformly altered in terms of extent or type.

Compositional analyses also include analytical error (Ague and van Haren, 1996). Samples picked to represent protolith may yield significantly different results, due to variable composition. Simplified approaches using arithmetic averaging of geochemical data do not address this issue. Univariate geochemical datasets do not generally follow a Gaussian distribution model and standard statistical approaches are invalid for multivariate compositional data (Vistelius, 1960; Aitchison, 1986; Aitchison, 1989; Reimann and Filzmoser, 2000). The sample vs. sample approach of Grant (1986, 2005) also becomes laborious when handling many samples, as are commonly available at an advanced mineral exploration project or mining operation. Many computer programs have been developed to improve the speed of processing mass balance equations (Potdevin, 1993; Lopez-Moro, 2012), or to facilitate the selection of an immobile reference frame (Janousek et al., 2006; Carrasco and Girty, 2015). While useful, these approaches do not statistically represent compositional variability of sample populations and the uncertainty of mass balance results is not provided.

Recent work by Ahmed et al. (2019) addresses this issue by examining boxplots of sample data to assess the uncertainty of individual mass balance estimates and uses spreadsheets to speed up calculations. However the approach of Ahmed et al. (2019) does not provide a robust estimate of element change for the entire alteration domain. To address this issue, we apply the modified mass balance approach of Ague and van Haren (1996); this approach was selected because it features automation for dealing with large sets of samples, is statistically-robust, and provides a measure of confidence for results. An innovative use of these results is to relate them to the covariance of elements (as measured using PCA) and to furthermore derive 3-D representation of element enrichment and depletion. Results can then inform between geochemical data and the structural-mineralogical controls on mineralisation in orogenic Au deposits.

3. Case study area

The St Ives Au-Ni Camp is located near the township of Kambalda, Western Australia, 57 km south of Kalgoorlie. The St Ives area has produced over 12 Moz of Au to date, from multiple open pit and underground mines (Carolus, 2018). Discovered in 2009, the Hamlet underground mine occurs within the multi-million-ounce Argo-Athena-Hamlet shear complex (Fig. 1) in the southern portion of St Ives and is currently in production.

St Ives is in the Kambalda Domain of the Kalgoorlie Terrane, Yilgarn Craton, Western Australia (Czarnota et al., 2010). The greenstone stratigraphy of the Kambalda Domain comprises regionally metamorphosed mafic-ultramafic, felsic intrusive and clastic sedimentary units (Squire et al., 1998; Krapež and Hand, 2008; Czarnota et al., 2010). The Paringa Basalt, which hosts Hamlet (Fig. 2), is part of a regional high-Th siliceous basalt group (Barnes et al., 2012) with a type area located between Kalgoorlie and Kambalda. The Paringa Basalt comprises submarine pillowed and massive facies, some of which are thick and internally differentiated (Lesher, 1983). The major element compositions of the unit range from magnesian andesite to basalt with anomalously high Si content and include a component of fractionates and cumulates (Barnes et al., 2012). Regional greenschist facies metamorphism, overprinting the Paringa Basalt, is recorded by an assemblage of amphibole-chlorite-albite-plagioclase (Prendergast, 2007).

The Hamlet deposit is hosted entirely within the Paringa Basalt. This formation contains variolitic intervals and pillowed basalt flows up to tens of metres thick, and thicker differentiated dolerite units up to hundreds of metres. The formation grades from high-Mg basalt at the base, to more-evolved tholeiitic basalts at the top; these two geochemical domains are informally separated as Upper- and Lower-Paringa Basalt (Barnes et al., 2012; Walshe et al., 2014). As it is not always possible to separate these subunits visually during diamond drill core logging, logs contain codes for Upper- or Lower Paringa, or simply Paringa. Typically, they are discriminated into three informal subunits

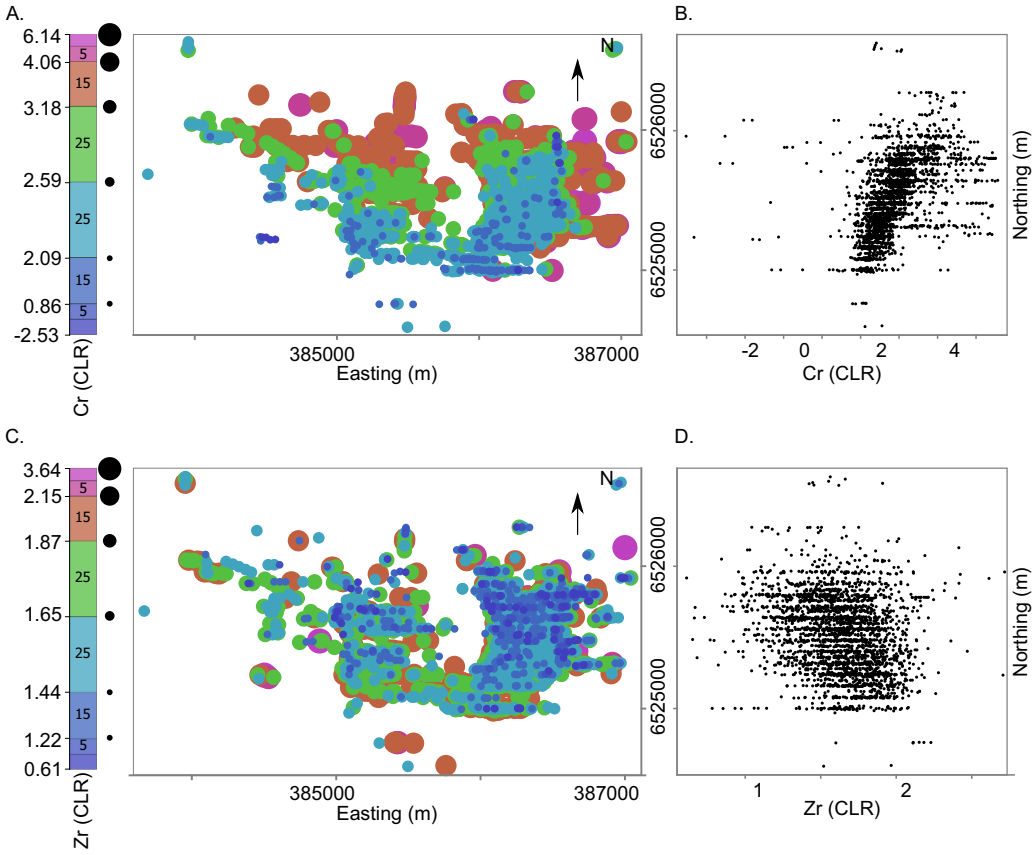

Fig. 4. Map of Cr and Zr values. Generally, Cr content increases from south to north, moving upwards through stratigraphy (A and B). Zirconium and other potentially immobile elements such as Hf, Sc, Ti, Nb, and P generally have a range of values across the Paringa Basalt subunits and do not significantly vary from south to north (C and D).

using whole rock geochemical data. These subunits are defined using Th-Cr-Ti ternary plots as the Upper, Middle, and Lower Paringa Basalt (Walshe et al., 2014).

Structurally, the Kambalda Domain is bound to the east by the Boulder-Lefroy Fault Zone and to the west by the Zuleika Shear Zone (Swager et al., 1995; Myers, 1997). Multiphase deformation associated with movement along these shear zones is manifested by five main deformation events (Blewett et al., 2010; Miller et al., 2010; McGoldrick et al., 2013b). Gold mineralisation is interpreted to have occurred during peak metamorphism, late in the deformation history, within second-order structures such as vein arrays, sinistral-reverse shear zones and thrust faults related to the episodic rupture of segments on the main faults (Nguyen et al., 1998; Cox and Ruming, 2004; Connors et al., 2005; Ruming, 2006; Miller et al., 2010).

The Hamlet Shear Zone cuts the Paringa Basalt as a steeply dipping, 5 m to 25 m wide zone of shear foliation (Fig. 2). The shear zone may be continuous, or a series of discrete narrow shears separated by undeformed basalt. Potassic alteration, in the form of biotite replacement of chlorite or pyroxene, is present as an envelope around veining in the shear zone (Fig. 3) ≤15 m thick. Gold mineralisation at Hamlet comprises quartz and carbonate vein arrays with associated biotite-carbonate-albite-sulfide wall-rock alteration in the shear zone. Pervasive, pale yellow-brown albite is most strongly developed around stockwork quartz-albite veining and quartz-albite matrix breccias (Fig. 3). When plotted in 3-D the samples with the highest Au grades occur along multiple trends within the Hamlet Shear Zone, with no single dominant orientation.

4. Methods

4.1. Initial data and pre-processing

The unfiltered database used in this study contains 6051 samples and 61 elements from whole-rock analyses. Multi-element assays were produced using a four-acid digest (Activation Laboratories' ME-MS61 procedure in Perth, Western Australia; Appendix A. Dataset QAQC). Whole-rock multi-element geochemistry is from both Inductively Coupled Plasma (ICP) Mass Spectrometry (-MS) and Atomic Emission Spectroscopy (-AES) analyses. The ICP dataset contains 60 elements Ag, Al, As, Ba, Be, Bi, Ca, Cd, Ce, Co, Cr, Cs, Cu, Dy, Er, Eu, Fe, Ga, Gd, Ge, Hf, Ho, In, K, La, Li, Lu, Mg, Mn, Mo, Na, Nb, Nd, Ni, P, Pb, Pr, Rb, Re, S, Sb, Sc, Se, Sm, Sn, Sr, Ta, Tb, Te, Th, Ti, Tl, Tm, U, V, W, Y, Yb, Zn, Zr. Gold was analysed by fire assay (Appendix A. Dataset QAQC). Values less than analytical limit of detection (LOD; censored values) were substituted with values half of detection limit (Grunsky and Smee, 1999; Carranza, 2011) and are listed in Appendix A. When < 30% of element values are censored, replacement of censored values with values half of detection limit has been shown to have minimal effect on the mapping and interpretation of multi-element anomalies related to mineralisation (Carranza, 2011).

Principal components analysis (Pearson, 1901; Jolliffe, 2011) was used to produce geochemical groups in ioGAS™. Conventional algebraic operations and statistical calculations applied to compositional data lead to incorrect results (Pawlowsky-Glahn et al., 2015). This is because chemical compositional data are closed, sum to a constant value, and only contain relative information. Therefore correlation coefficients calculated on raw compositional data are not valid (Aitchison, 1986; Pawlowsky-Glahn et al., 2015). To address this, element concentrations were transformed before PCA using the centred log-ratio (CLR) transform (Aitchison, 1986; Aitchison, 2008). A subset of samples did not include the elements Dy, Er, Eu, Gd, Ho, Lu, Nd, Pr, Se, Sm, Tb, Tm, or Yb as part of analytical batches. These elements were omitted from transformation. The final list of CLR transformed elements (n = 48) were: Ag, Al, As, Au, Ba, Be, Bi, Ca, Cd, Ce, Co, Cr, Cs, Cu, Fe, Ga, Ge, Hf, In, K, La, Li, Mg, Mn, Mo, Na, Nb, Ni, P, Pb, Rb, Re, S, Sb, Sc, Sn, Sr, Ta, Te, Th, Ti, Tl, U, V, W, Y, Zn, and Zr.

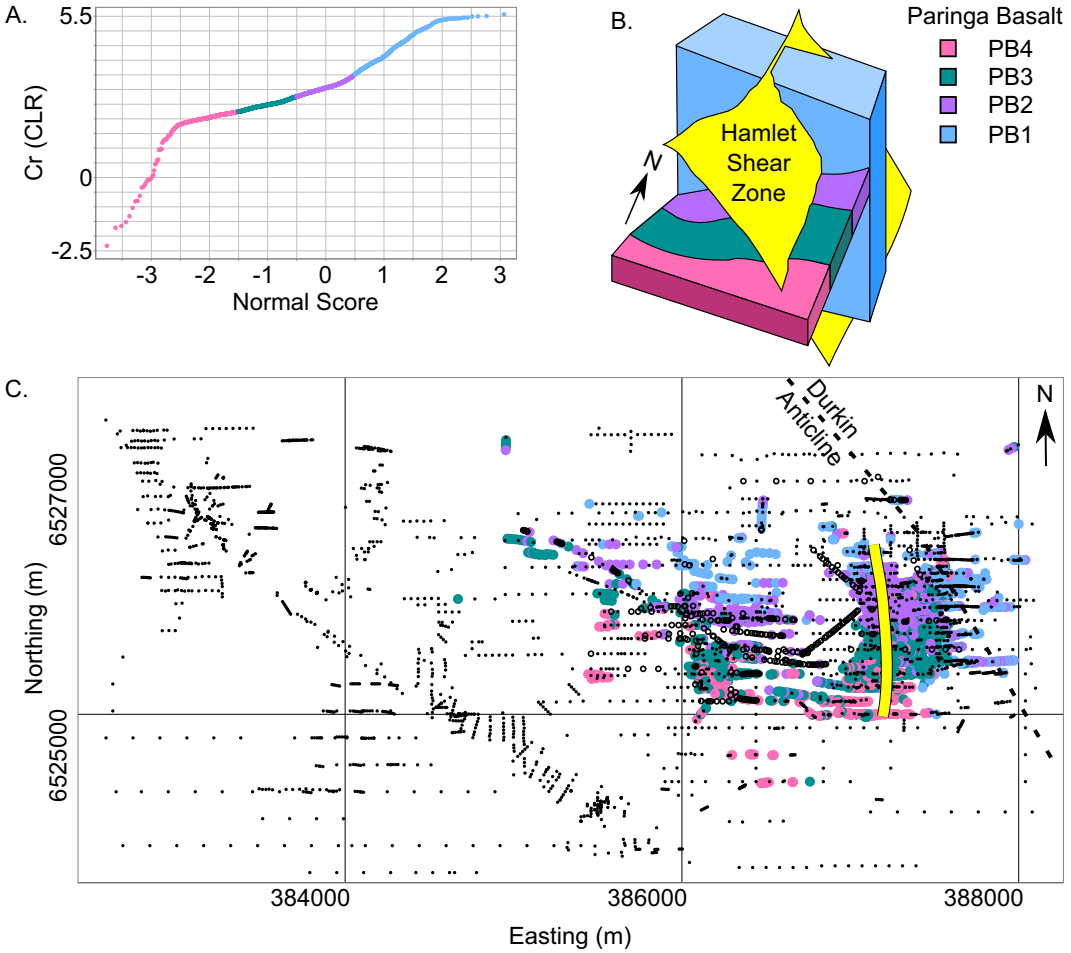

Fig. 5. Manual redefinition of four subunits of Paringa Basalt (PB1—PB4) using a probability plot of Cr and normal scores of −1.0, 0.0, and 1.0 (A.). The Hamlet Shear Zone crosscuts these subunits at a high angle (B. and C.). Samples have been projected vertically to surface, for ease of viewing. Samples that are not Paringa Basalt are marked as black points; samples omitted from CLR calculations are marked as open circles.

Mass balance estimates require characterisation of least-altered protolith samples for comparison with corresponding altered samples. We produced the required lithological groups using geochemical discrimination plots in ioGAS™. Mass balance calculations were performed using the Python programming language with the numpy and pandas library modules. Compositional data were used for mass balance calculations (not CLR transformed data) because the mass balance equations use element ratios, an appropriate method to deal with closure issues (Grant, 1986; Ague and van Haren, 1996; Grant, 2005). Finally, assessment of mass balance data in 3-D was performed using Datamine™ and Leapfrog™ software.

4.2. Identification of least-altered, weathered, and variably altered samples

Visual core logging data was present for most, but not all, samples. This information included stratigraphic unit (42 classes), regolith type (12 classes), and rock type (48 classes). A variety of fields denoting logged mineralogy were also available. A representative subset of Hamlet basalt samples was extracted using common logging codes. First, least weathered rocks were identified using the regolith column (3170 samples not designated as part of the regolith profile). Next, logged stratigraphic entity was used to isolate samples logged as Paringa Basalt (3489 samples marked as Upper-, Lower-, or un-differentiated Paringa Basalt), and logged rock type was used to select only samples marked as mafic (3473 samples). Twenty-seven samples with Ni < 50 ppm plot west of the Hamlet study area indicating these were mis-logged as Paringa Basalt, and they were rejected. A total of 3024 records were present after filtering by rock type. However, after omitting samples with missing analyses (i.e., where elements of interest had not been assayed for (see Appendix A. Dataset QAQC)), the final number of transformed samples was 2726.

The Paringa Basalt is geochemically heterogeneous and so was divided into smaller geochemical domains related to igneous fractionation. The variation in Cr composition of the Paringa Basalt is gradational from north to south (Fig. 4). A probability plot of Cr CLR produces approximately similar sized subunit volumes using normal score thresholds of −1.0, 0.0, and 1.0 (Fig. 5). These thresholds divide the Paringa Basalt from stratigraphic base to top into PB1 (n = 433 samples), PB2 (n = 930 samples), PB3 (n = 931 samples), and PB4 (n = 432 samples).

Once samples had been grouped into subunits, least-altered and Au-associated samples needed to be separated (Fig. 6). First, Au and Te LOD values (Au = 0.0005 ppm and Te = 0.025 ppm) were used to identify unmineralised samples. Next, samples along the albite trend of a Na (mol)/Al (mol) vs. K (mol)/Al (mol) plot (Davies and Whitehead, 2006, 2010) were selected to isolate samples likely to contain K or Na-bearing alteration minerals, i.e., albite or biotite. The alkali index (molar ratios of Na/Al and K/Al; Fig. 6A) is an effective tool for identifying major alteration types in Archaean orogenic systems (Davies and Whitehead, 2006; Prendergast, 2007; Davies and Whitehead, 2010). Sodic and potassic alteration assemblages are common in orogenic Au deposits and are coincident with Au mineralisation at Hamlet. Weathering of mafic igneous rocks can be discriminated on a ternary plot of Al_2O_3-CaO-K_2O [mol%] (Nesbitt and Young, 1984) (Fig. 6B).

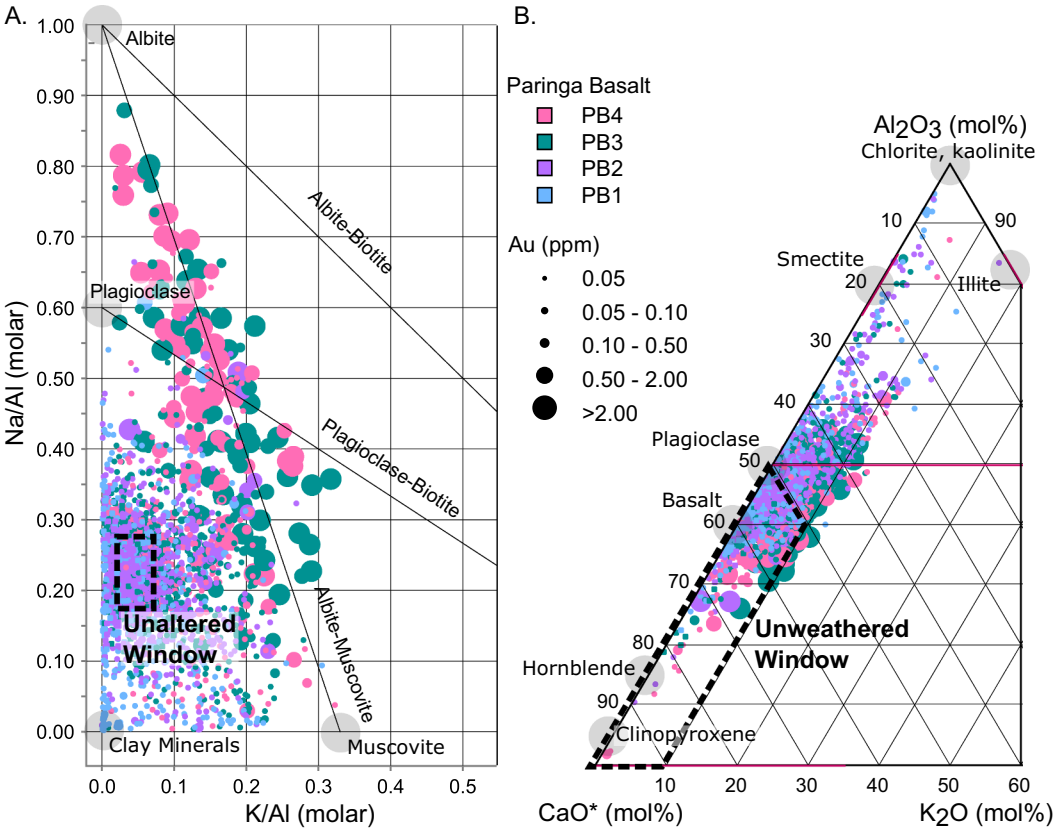

Fig. 6. Manual assessment of alteration and weathering. Unaltered samples have been chosen as having Au = 0.05 ppm and Te = 0.025 ppm (i.e., both LOD), plotting within the unaltered and unweathered windows. A. Na/Al (molar) vs K/Al (molar) diagram (modified form Davies and Whitehead, 2006) to assess alteration. Samples plotting outside a bounding box of 0.020–0.060 K/Al and 0.175–0.275 Na/Al are considered altered. B. Al_2O_3-CaO-K_2O weathering trend ternary diagram (after Nesbitt and Young, 1984). The window of unweathered samples ranges from 0–50% Al_2O_3 and 0–10% K_2O in the ternary space.

Table 1
Description of variables comprising Eq. (1).
Modified from Grant (1986).

Variable	Description
C^A	Concentration of an element in altered rock
C^O	Concentration of an element in least-altered rock
M^A	Mass of altered rock
M^O	Mass of least-altered rock
Ci^A	Initial concentration of element in altered rock
Ci^O	Initial concentration of element in least-altered rock
C^A/C^O	A proportion representing the change in concentration (addition or depletion) of an element
M^A/M^O	Isocon reference proportion; the geochemical baseline determined by user-selected immobile elements
Ci^A/Ci^O	Initial concentration of an element in the altered sample as a proportion of an unaltered sample

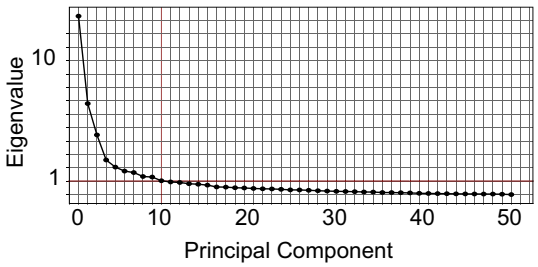

Fig. 7. Scree plot of PCs against eigenvalues, to assess which components contain the most variability. The threshold line of 1 marks PC10; the first 10 PCs account for 75.9% of the variance.

Linear combinations of elements reflecting mineralogy can be more effectively identified using PCA than by through user-defined groups (Grunsky et al., 2014). This approach can use geochemical data to inform rock composition (Grunsky and Smee, 1999; Grunsky et al., 2014), degree of weathering in regolith (Ohta and Arai, 2007; de Caritat and Grunsky, 2013), and alteration (Loughlin, 1991; Fisher et al., 2014; Caciagli, 2015; Gazley et al., 2015). A benefit of PCA is that the dimensions of data are reduced, and elements that are covariant can be identified. Multivariate geochemical data represented in Principal Component (PC) space are transformed so that the axis of greatest variance becomes the first PC, the axis of second-greatest variance becomes PC2, and so on. A triaxial plot of PC1-PC2-PC3 will thus summarise the greatest amount of variance in the dataset and be a more comprehensive summary of that dataset than a plot of any three original variables.

4.3. Statistically-based mass balance estimates

Our approach to calculating mass balance follows the method of Ague and van Haren (1996). The results obtained using this method produce mathematically-appropriate average estimates of element mass change for an alteration domain, bounded by confidence limits. Averaged compositions for representative samples can also be extracted and used to solve mass balance equations for original samples. Results can then be plotted spatially to interpret patterns of conventional mass balance in 3-D.

Gresens' (1967) equation, rearranged by Grant (1986), is shown in Eq. (1), and the variables making up the equation are defined in Table 1.

Table 2
Table of scaled eigenvectors for PC1-PC10, calculated from CLR transformed geochemical data (n = 2726 samples). Values range from 1 (perfect correlation) to −1 (perfect anticorrelation). Each PC has been sorted individually, so that element associations appear at the positive and negative ends of each PC.

PC3		PC4		PC5		PC6		PC7		PC8		PC9		PC10	
Rb	0.69	Be	0.54	Sb	0.47	Mo	0.49	Sn	0.49	Sr	0.41	Cu	0.52	As	0.50
Cs	0.69	Cr	0.52	Pb	0.42	Sb	0.32	In	0.38	Pb	0.37	S	0.32	P	0.20
Tl	0.64	Ni	0.45	Mo	0.34	V	0.31	As	0.32	Sn	0.32	Cr	0.29	Cu	0.20
Ba	0.63	Li	0.41	As	0.30	As	0.26	Zn	0.28	In	0.32	Ni	0.23	Cd	0.20
K	0.63	Mg	0.27	La	0.27	W	0.26	Li	0.20	Bi	0.25	Co	0.20	S	0.16
Li	0.42	Na	0.27	Cs	0.26	Sc	0.24	Bi	0.18	Na	0.22	Sc	0.16	Zr	0.16
Sc	0.30	Sr	0.25	Ce	0.24	Re	0.23	Hf	0.17	Be	0.18	Th	0.14	Hf	0.15
Fe	0.27	Co	0.22	Tl	0.23	Ti	0.22	Re	0.16	Ba	0.18	V	0.13	Sr	0.11
V	0.23	W	0.20	Sn	0.20	Ca	0.16	Zr	0.15	V	0.15	U	0.10	Ti	0.09
Mn	0.21	As	0.18	Th	0.17	Na	0.15	Ti	0.15	Cu	0.14	La	0.09	Na	0.07
Co	0.21	Al	0.17	U	0.16	Al	0.15	Ta	0.09	Al	0.12	Na	0.08	Li	0.07
Y	0.17	Ga	0.15	Zn	0.14	K	0.09	Nb	0.09	K	0.11	Ta	0.08	Ca	0.07
Cr	0.16	Au	0.12	Ba	0.13	Ba	0.09	W	0.09	Ga	0.11	Al	0.08	Zn	0.04
Ni	0.15	Hf	0.07	Ni	0.12	Rb	0.08	P	0.08	Ca	0.09	Bi	0.08	Pb	0.03
P	0.14	Pb	0.07	P	0.12	Mn	0.08	Be	0.04	Sc	0.08	Ce	0.06	Tl	0.03
Ge	0.13	Sb	0.04	Cr	0.11	Ga	0.07	V	0.04	Sb	0.07	Ti	0.05	V	0.01
Ti	0.11	Ti	0.02	Rb	0.10	Ta	0.06	Y	0.04	Ti	0.07	Re	0.05	Al	0.00
Al	0.08	P	0.02	Re	0.08	Cu	0.06	Tl	0.03	Rb	0.07	Nb	0.04	Co	−0.01
Mg	0.07	Zr	0.01	Cd	0.07	Nb	0.06	Na	0.03	Cd	0.05	Ga	0.03	In	−0.01
Zr	0.06	Tl	0.00	Ge	0.04	Y	0.06	Ga	0.03	Tl	0.04	Te	0.03	Nb	−0.01
Zn	0.06	V	0.00	In	0.04	Fe	0.03	Sb	0.02	Cr	0.04	Y	0.02	Mg	−0.02
Nb	0.05	Cs	−0.01	Sr	0.01	Co	0.02	Co	0.01	Zn	0.02	Pb	0.01	Sb	−0.02
Hf	0.05	Th	−0.03	K	0.01	Sr	0.01	Mo	0.00	Co	0.02	Au	0.00	Mn	−0.02
Ta	0.04	Te	−0.04	Mg	0.01	Cs	−0.01	Au	−0.01	S	0.02	As	−0.01	Au	−0.03
Ce	0.03	K	−0.05	Co	0.00	P	−0.02	Ba	−0.01	Cs	0.02	Sb	−0.04	Cs	−0.03
Th	0.02	Nb	−0.06	S	−0.02	Tl	−0.02	Cs	−0.01	Ni	0.01	Cs	−0.04	Ta	−0.03
La	0.01	U	−0.06	Nb	−0.03	Ge	−0.05	Te	−0.02	Li	0.00	Ge	−0.04	Ag	−0.04
In	0.00	Ta	−0.06	Cu	−0.03	Mg	−0.05	Al	−0.03	Re	−0.02	Be	−0.05	Ni	−0.04
Ga	−0.02	La	−0.06	Ta	−0.04	S	−0.07	S	−0.06	Ag	−0.02	Tl	−0.07	K	−0.05
Re	−0.05	Ce	−0.06	Bi	−0.06	In	−0.09	Fe	−0.06	Ta	−0.02	In	−0.07	Ce	−0.05
U	−0.05	Ba	−0.07	W	−0.07	Cr	−0.09	K	−0.06	P	−0.03	Rb	−0.08	Ba	−0.06
Ca	−0.07	Rb	−0.07	Y	−0.10	Au	−0.12	Sc	−0.06	Nb	−0.03	Mg	−0.08	Be	−0.07
Cu	−0.12	Ge	−0.07	Fe	−0.13	Be	−0.12	Ag	−0.06	Y	−0.03	Hf	−0.08	Ga	−0.07
S	−0.17	Mo	−0.08	Be	−0.13	Ni	−0.13	Rb	−0.06	Mg	−0.06	Fe	−0.08	Fe	−0.07
Sn	−0.21	Re	−0.08	Na	−0.14	Ag	−0.14	Ni	−0.11	Te	−0.07	Ag	−0.09	Rb	−0.07
Te	−0.21	Sc	−0.12	Hf	−0.15	Cd	−0.15	Cu	−0.11	Mn	−0.08	P	−0.09	Y	−0.08
Be	−0.22	Sn	−0.14	Al	−0.16	Zr	−0.20	Ge	−0.12	Fe	−0.08	Ba	−0.09	La	−0.08
Ag	−0.26	Ca	−0.20	Zr	−0.16	Hf	−0.21	Cr	−0.13	Ge	−0.13	Zr	−0.10	Th	−0.08
As	−0.27	Bi	−0.21	Mn	−0.18	Pb	−0.22	Cd	−0.15	Au	−0.15	K	−0.12	Sc	−0.09
Au	−0.27	Zn	−0.21	Ti	−0.19	Te	−0.23	Mn	−0.17	Ce	−0.19	Mo	−0.13	Cr	−0.09
Pb	−0.33	In	−0.21	Ga	−0.21	U	−0.24	Ce	−0.17	Th	−0.21	Sn	−0.15	U	−0.10
Cd	−0.33	Mn	−0.22	Ca	−0.22	Li	−0.24	La	−0.18	U	−0.21	W	−0.15	Te	−0.17
Sr	−0.36	Fe	−0.23	Li	−0.22	Zn	−0.25	Th	−0.19	Hf	−0.21	Li	−0.16	Ge	−0.20
Bi	−0.38	Ag	−0.24	Ag	−0.24	Sn	−0.25	U	−0.21	La	−0.22	Sr	−0.21	W	−0.21
Na	−0.38	Cd	−0.31	V	−0.25	Th	−0.26	Mg	−0.21	Zr	−0.24	Zn	−0.29	Sn	−0.21
Mo	−0.41	Y	−0.34	Sc	−0.25	Ce	−0.31	Pb	−0.23	Mo	−0.24	Mn	−0.30	Bi	−0.26
Sb	−0.43	S	−0.47	Au	−0.46	La	−0.32	Sr	−0.46	As	−0.26	Cd	−0.35	Mo	−0.33
W	−0.52	Cu	−0.62	Te	−0.49	Bi	−0.33	Ca	−0.54	W	−0.28	Ca	−0.35	Re	−0.36

$$\frac{C^A}{C^O} = \left(\left(\frac{M^A}{M^O}\right) * \left(\frac{Ci^A}{Ci^O}\right)\right) - 1 \quad (1)$$

Quantification of mass changes in an open-system requires identification of one or more immobile elements (Gresens, 1967; Pearce and Cann, 1973; Grant, 1986). High Field Strength Elements (HFSE) and Rare Earth Elements (REE) are typically immobile during alteration (Pearce and Cann, 1973; Pearce, 1996). Whether an element has actually been immobile can be examined using the ratio of $C_i^{\circ}/C_i^{'}$, which will be similar for all immobile elements (e.g., Grant, 1986; Ague and van Haren, 1996).

Bootstrapping is a statistical, non-parametric re-sampling technique (Efron, 1979). Synthetic sample sets created using the bootstrap are used to better represent incomplete data distributions and to obtain estimates of summary statistics for non-normal geochemical distributions. Bootstrapping selects many samples at random, allowing duplicates, from a matrix. For each of our four protolith rock suites (PB1, PB2, PB3, and PB4) we first produced two synthetic sets of samples: one representing least-altered rocks and one representing selected altered rocks. For each sample set, 5000 bootstrapped records were created.

The synthetic protolith and altered sample sets for each subunit were then used to calculate the Aitchison Measure of Location (AML). The AML is a measure of central tendency which uses a geometric mean to determine an average value for geochemical distributions with non-normal probability distributions (Aitchison, 1989; Woronow and Love, 1990). The geometric mean is defined as the n^{th} root of $(x_1 * x_2 * \ldots * x_n)$ and is used for non-normal distributions when a conventional arithmetic mean is not mathematically appropriate.

The resulting probability distribution of AML values is normal, and the mean AML value for each element can be used to create a representative averaged sample for each set of samples. From these, immobile element candidature can be assessed, and mass balance values can be calculated. The bootstrapped AML method is repeated for the matrix of samples representing the protolith domain, and that which

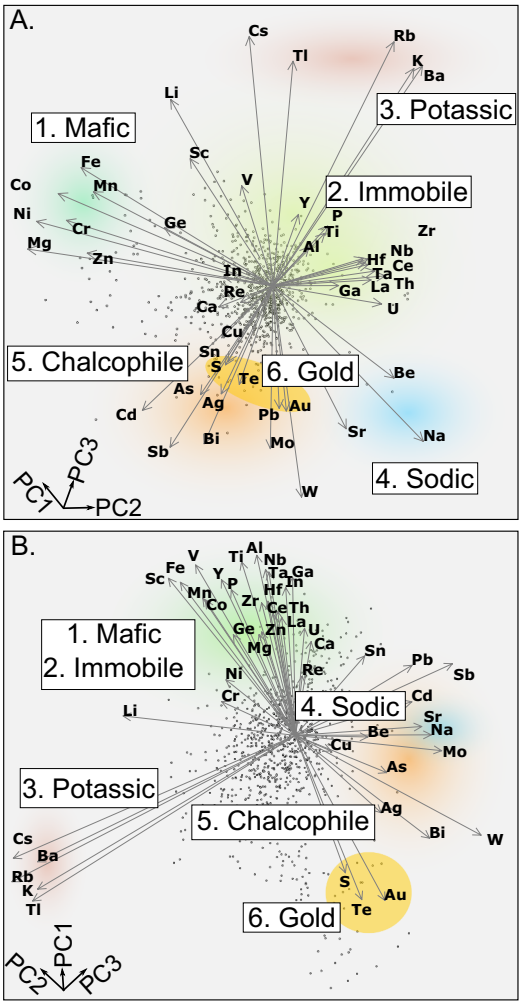

Fig. 8. Results of PCA plotted in PC1-PC2-PC3 space. The three PCs account for 51.2% of the variance. Axes have been rotated to best illustrate clusters of eigenvectors. Plots of PC1 vs. PC2 and PC1 vs. PC3 space are given in Appendix B. Principal Component Supplement.

represents the alteration subdomain. The two derived matrices are then used to produce a matrix of mass change values which reflect the original probability distributions (Ague and van Haren, 1996).

$$(\overline{C}_1, \overline{C}_2, \ldots \overline{C}_M) = \frac{g_1, g_2, \ \ldots, g_M}{\sum_{m=1}^{M} g_M} \tag{2}$$

where $\overline{C}_M$ is the concentration of constituent m, and M is the total number of constituents used to calculate the geometric mean of constituent m (g_m):

$$g_m = \exp\left[N^{-1} \sum_{n=1}^{N} \ln(c_{n,m})\right] \tag{3}$$

The AML vectors are denoted AML° (protolith suite) and AML' (altered suite) using Eq. (2), yielding:

$$AML^{\circ} = \overline{C}_1^{\circ}, \overline{C}_2^{\circ}, \ \ldots, \overline{C}_M^{\circ}, \tag{4}$$

$$AML' = \overline{C}_1', \overline{C}_2', \ \ldots, \overline{C}_M', \tag{5}$$

Best estimates of mass change are then calculated:

$$\widehat{T} = \left(\frac{\overline{C}_i^{\circ}}{\overline{C}_i'}\right) - 1, \tag{6}$$

$$\widehat{\tau}^j = \left(\frac{\overline{C}_i^{\circ}}{\overline{C}_i'}\right)\left(\frac{\overline{C}_j'}{\overline{C}_j^{\circ}}\right) - 1, \tag{7}$$

where $\widehat{T}$ is the total mass change and $\widehat{\tau}^j$ is the mass change for mobile species j, calculated using replicate bootstrap analysis.

Immobile elements are identified by constant inter-element ratios for like lithology. Straight lines on scatter plots are conventionally used (Pearce, 1996; Piercey et al., 2002), but the bootstrapped AML matrices provide robust values of $\overline{C}_i^{\circ}/\overline{C}_i'$ and allow comparison between elements. For example, elements with similar proportions of $\overline{C}_i^{\circ}/\overline{C}_i'$ appear as a plateau of values. The geometric mean of immobile element proportions $\overline{C}_i^{\circ}/\overline{C}_i'$, the Geometric Mean Best Estimate (GMBE), represents the immobile-element reference frame from which element addition and depletion are then calculated. A geometric mean is used to calculate the GMBE, as literature suggests it provides better results than an arithmetic mean for ratio quantities (Spiegel, 1961).

Next, the GMBE immobile reference frame is used to solve Eq. (7). Five-thousand solutions are generated (as there are 5000 samples is the protolith matrix and 5000 corresponding samples in the altered sample matrix). A geometric mean is used to produce a single mass balance estimate for the alteration domain, and 95% confidence limits are placed about this value. This representation provides an averaged measure of element mass change and a representation of uncertainty arising from geochemical heterogeneity. Confidence limits spanning the 0% mass change line indicate that elements cannot be stated as having had mass gain or loss and cannot be used reliably to quantify or represent element mass balance. Finally, the geometric mean of values for the representative protolith of each subunit is used to calculate mass balance for each appropriate altered sample in the original dataset. The results are plotted spatially for interpretation in 3-D.

5. Results

5.1. Principal component element patterns

Ten PCs were selected using the change in slope of a scree plot (Fig. 7) and account for 75.9% of data variance for CLR-transformed data (Appendix B. Principal Component Supplement). The relative contributions of elements to each PC are given in Table 2 and is coloured to indicate groups of elements with similar covariance.

Element eigenvectors are plotted in 3-D using PC1—PC3 as axes (Fig. 8). Six groups of elements are defined by similar vector orientation and magnitude: (1) relatively immobile elements, e.g., Ce, Ga, Hf, Nb, La, Ta, Th, and Zr; (2) elements associated with mafic rocks, Ca, Co, Cr, Fe, Ge, Mg, Mn, Ni, and Zn; (3) elements related to potassic alteration: Ba, Cs, K, Rb, and Tl; (4) elements related to sodic alteration: Be, Na, and Sr; (5) chalcophile elements, including Bi and Sb; and (6) Au, Te, and S.

5.2. Immobile element trends

Scatter diagrams were used to examine elements with a sympathetic relationship to Zr (c.f., Piercey et al., 2002) by plotting Zr against Al, Ga, Hf, Nb, Sc, Ta, Th, V, Y, Cr, and Ni. Zirconium vs. Hf produced the most linear trend (Fig. 9A). These elements were selected to provide the immobile element reference frame, used for all mass balance calculations, as they have $\overline{C}_i^{\circ}/\overline{C}_i'$ proportions similar to those of Cr, La, Ce, and Ga (Fig. 10).

5.3. Alteration and weathering discrimination

The alkali index (molar Na/Al and K/Al) shows that the highest Au grade samples cluster along the albite-muscovite tie line (Fig. 6A); samples associated with this trend were tagged to represent the altered end-member for mass balance study. Existing work in the St Ives region,

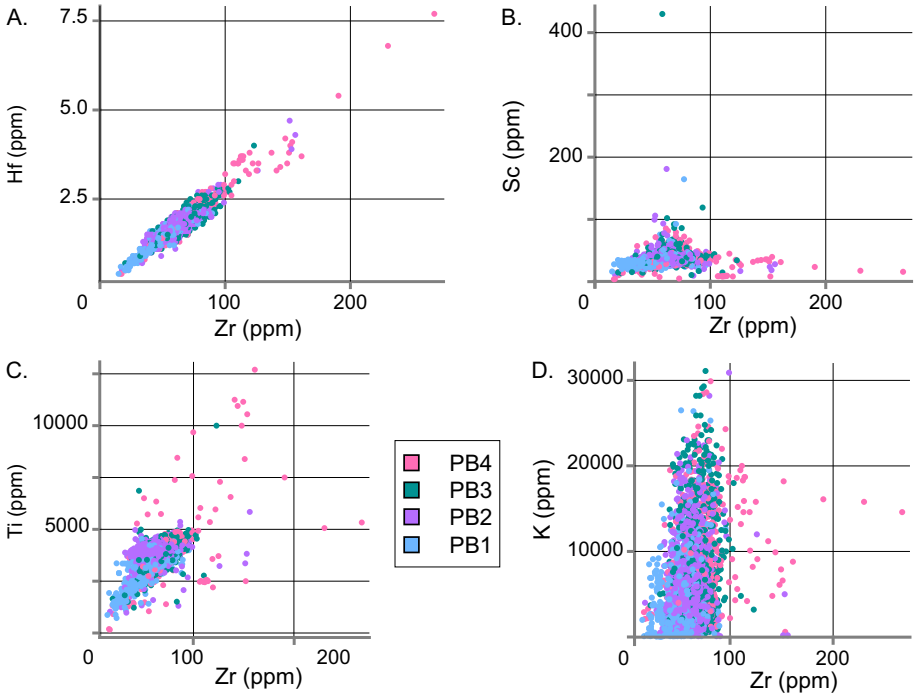

Fig. 9. Scatter plots to assess immobility of elements. A linear trend between Zr and another element (e.g., Hf) suggests similar proportions between the elements across variably altered and weathered samples. Samples identified as subunits PB1—PB4 are shown. The elements Sc and Ti are typically considered to be immobile but here do not exhibit a strong linear correlation with Zr. Potassium is an example of a fluid-mobile element.

which predates the discovery of Hamlet, suggests that unaltered mafic rocks (including, but not limited to the Paringa Basalt) have alkali index ranges of $0 \leq K/Al \leq 0.07$ and $0.2 \leq Na/Al \leq 0.4$ (Prendergast, 2007). We instead selected least-altered boundaries of $0.02 \leq K/Al \leq 0.06$ and $0.175 \leq Na/Al \leq 0.275$, which represent the highest point density for unmineralised samples not occurring within the envelope of the Hamlet Shear Zone (Fig. 6A).

Weathering of mafic igneous rocks examined on a ternary plot of Al_2O_3-CaO-K_2O (Nesbitt and Young, 1984), and threshold values of $Al_2O_3/CaO = 0.5$ and $CaO/K_2O = 0.9$ were used to isolate least-weathered samples (Fig. 6B). Bounds for both plots were selected based on the highest point density of samples logged to be least-altered and least-weathered. A second filtering to exclude weathered samples was then done. Spatial examination of PC5 and PC6 (Table 2) indicate incipient weathering correlated with PC5 > 1 and PC6 > 1. Samples with these values tended to be close to surface, with horizontal continuity, and were omitted from further examination. The resulting number of least-altered and altered sample pairs for PB1 (nine and 30), PB2 (124 and 22), PB3 (141 and 83), and PB4 (31 and 89) exceed the number of pairs demonstrated for bootstrapped mass balance estimations in the original study (seven least-altered samples and six altered samples; Ague and van Haren, 1996).

5.4. Mass balance

A reference frame defined by Zr and Hf was used for mass balance calculations, for all subunits (Fig. 10). The bootstrapped GMBE reference frame values for subunits were each less than one: PB1 = 0.77; PB2 = 0.77; PB3 = 0.99; and PB4 = 0.9. Total mass loss estimates for the subunits are: PB1 = −23%; PB2 = −22%, PB3 = −1%; and PB4 = −10%.

Mass balance estimates for representative alteration subdomains are presented in Fig. 11 and Table 3. Results indicate that Ba, Bi, Cs, K, Na, Rb and Tl are enriched in samples along the Na-K alteration trend, for all subunits. Mass addition for strongly added elements is on the order of hundreds of percent (Table 3). Note that elements that tend to have very low or LOD values in protolith samples (e.g., Au, Te, and S) yield erroneously high results. Calcium, Cd, Co, Cu, Fe, Ge, Mg, Mn, Sc, Sb, Y, and Zn appear in the depleted region of the mass balance plots for all subunits. Mass depletion for strongly removed elements is about 40–60% (Table 3).

A sample-by-sample comparison of original data versus mass balance values is presented in Fig. 12. Original concentration data (ppm) are plotted against derived mass balance values (%) as probability–probability (P-P) plots. Raw data have been sorted in ascending order and represent the independent variable and expected probability distribution of samples. Mass balance values on the dependent axis are plotted by corresponding sample number. Deviations from a straight-line linear trend indicate that the mass balance function is not providing a linear rescaling of the original concentration data.

Mass change estimates are calculated for each original sample of Paringa Basalt using results from the *AML′* of corresponding subunits. Results are shown on long-sections for a selection of these elements in Fig. 13. Potassium (Fig. 13A) suggests multiple orientations for element enrichment defined by smaller clusters of values with ranges up to about 300 m within the shear plane. Sodium (Fig. 13B) shows strongest addition values forming a zone which plunges towards the south-southeast. Calcium (Fig. 13C) depletion appears to correlate to zones of K and Na enrichment. Bismuth (Fig. 13D), like K, displays multiple orientations at short range (less than about 300 m).

6. Discussion

Paringa Basalt samples can be split into six geochemical groups based on PC eigenvector magnitude and direction (Fig. 8). These groups are categorised by electrochemical character and geological observation of the case study area as: (1) elements that are typically immobile; (2) elements generally associated with mafic rocks; (3) elements related to K alteration; (4) elements related to Na alteration; (5) chalcophile elements; and (6) elements strongly associated with Au mineralisation. These groups provide an initial understanding of Paringa Basalt geochemistry at Hamlet, as a basis for mass balance calculations and the interpretation of results.

6.1. Discrimination of Paringa Basalt subunits

The Paringa Basalt is fractionated from stratigraphic base to top (Barnes et al., 2012; Walshe et al., 2014), and so must be separated into

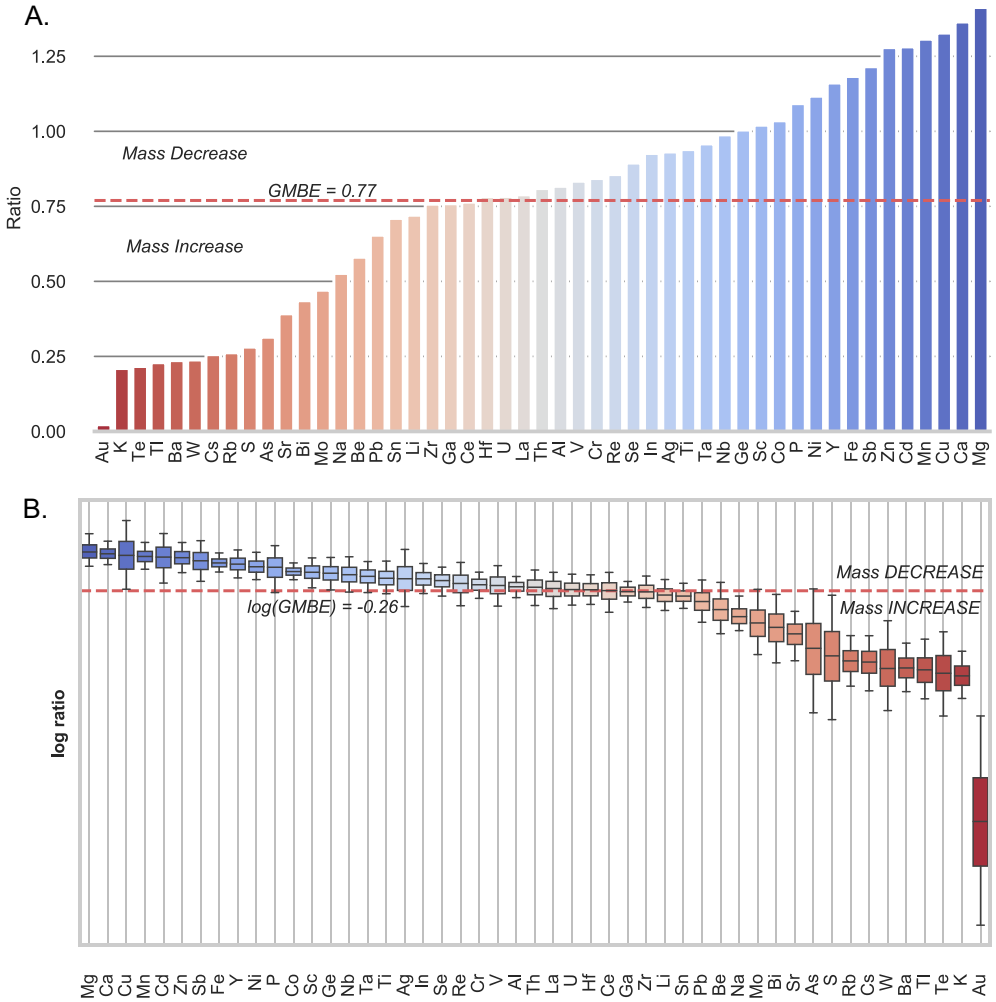

Fig. 10. Example plots to assist the selection of immobile element reference frame, after Ague and van Haren (1996). Element ratios ($\overline{C}_i^{\circ}/\overline{C}_i'$) are plotted as histograms (A) and logged box-and-whisker plots (B) to visually select likely immobile elements with similar isocon slopes (i.e., ratios). Data shown here represent the Na-K alteration trend in subunit PB3. Error bars are 95% confidence limits.

more geochemically similar subunits to inform mass balance calculations. Elements traditionally used for mafic volcanic rock discrimination include Ti, Zr, Y, Nb, Ce, Ga, and Sc (Cann, 1970; Floyd and Winchester, 1978; Pearce, 1996). However, their use in discriminating Paringa Basalt subunits is nominal because they are not significantly partitioned between the subunits. Previous workers in the Hamlet area used Th-Cr-Ti ternary discrimination plots to separate Paringa Basalt subunits (Walshe et al., 2014), although the Th and Ti axes do not influence the thresholds used (i.e., only Cr separates the respective subunits). However, a probability plot of CLR transformed Cr (or Ni) allows a straightforward alternative separation of four Paringa Basalt subunits, with Cr content decreasing from north to south (Fig. 4; Fig. 5). The distribution of the subunits compares favourably to previously mapped bedrock geology, where subunits of Paringa Basalt are folded about the Durkin Anticline (Fig. 1).

6.2. Fractionation trends of immobile elements

The classically immobile elements Al, Ce, Ga, Hf, La, Nb, P, Sc, Ta, Th, Ti, V, Y, and Zr (e.g., Pearce and Cann, 1973; Wood, 1980; MacLean, 1990; Jenner, 1996; Rollinson, 2014) group together in PC space of the Hamlet data, indicating a high degree of correlation between these elements despite overprinting alteration and weathering (Table 2 and Fig. 8). Except for Hf, these elements do not exhibit a strong linear correlation with Zr (e.g., Fig. 9). While Zr and Hf are also the most evenly distributed across the case study area (Fig. 4) other immobile elements vary in concentration from north to south. The strong linear correlation between Zr and Hf (Fig. 9) may suggest a similar magmatic fractionation history, and/or a mutual host phase such as zircon.

Concentration ratio plots for immobile elements produce $\overline{C}_i^{\circ}/\overline{C}_i'$ ratios around the GMBE, as expected (Fig. 10A and B). This is because ratios should be like those of Zr and Hf, which define the immobile reference frame. However, there is a progression of values defined by the immobile elements, creating a slope of estimates which influence mass balance results. This gradation could indicate either element mobility during alteration or variation within subunits (e.g., due to fractionation). As previously described, the Paringa Basalt is chemically fractionated (Barnes et al., 2012; Walshe et al., 2014), so mass change estimates for immobile elements are spurious, a result of primary gradational chemical composition of the basaltic sequence. Therefore, the gradation of mass balance estimates, and corresponding slope on Fig. 11, is interpreted to represent fractionation of immobile elements in basalt host rocks, rather than an alteration effect.

6.3. Geochemical changes associated with Au mineralisation

Previous element mobility studies were undertaken for mafic rocks near Hamlet, in the attempt to understand the implications of element mobility for Au exploration. These studies either infer mass change

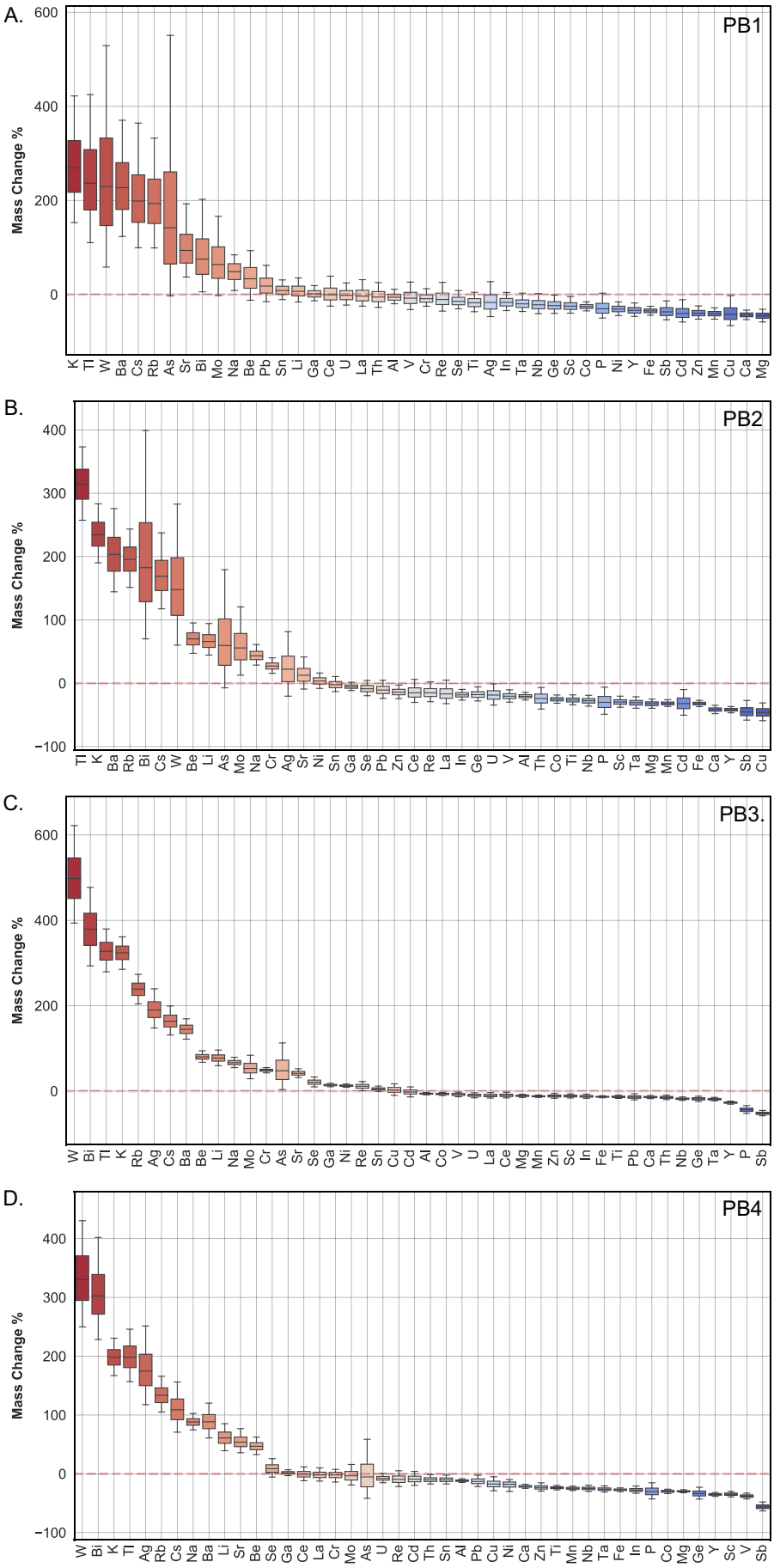

Fig. 11. Mass balance estimates and confidence limits for each subunit (PB1—PB4), calculated against samples in respective Na-K alteration zones. Confidence limits are to 95%, shown as box-whiskers. Box means represent the geometric mean calculated from 5000 bootstrap samples. Geometric mean values are also shown in Table 3. Elements are ordered from strongest alteration to most weak. Elements with confidence limits spanning zero mass change indicate either high heterogeneity in the protolith or altered sample sets, or minor variation between these sample sets. When mass balance estimates span 0%, no statistically relevant estimate can be assigned.

Table 3
Mass balance estimates for samples within the Hamlet Na-K alteration trend, calculated as the geometric mean of bootstrapped mass balance results. Warm colours indicate calculated element enrichment, while cool colours indicate element depletion. Mass balance estimates with confidence limits that do not span 0% are given in bold. In contrast, mass balance estimates with confidence limits that span 0%, are marked by italics.

	PB1			PB2			PB3			PB4		
	Mean	5% Conf.	95% Conf.	Mean	5% Conf.	95% Conf.	Mean	5% Conf.	95% Conf.	Mean	5% Conf.	95% Conf.
Au	**3352**	**583**	**16864**	**3704**	**1121**	**11870**	**138962**	**86538**	**218582**	**61418**	**32847**	**111047**
K	**269**	**153**	**422**	**Te**	**664**	**297**	**1376**	**Te**	**1298**	**1031**	**1619**	**Te**	**944**	**720**	**1209**
Te	**255**	**88**	**584**	**Tl**	**314**	**257**	**373**	**S**	**516**	**381**	**669**	**S**	**479**	**376**	**607**
Tl	**237**	**110**	**425**	**K**	**235**	**190**	**283**	**W**	**498**	**394**	**622**	**W**	**330**	**250**	**431**
W	**230**	**58**	**529**	**Ba**	**203**	**144**	**276**	**Bi**	**379**	**293**	**477**	**Bi**	**302**	**228**	**402**
Ba	**227**	**123**	**370**	**Rb**	**195**	**151**	**243**	**Tl**	**327**	**279**	**380**	**K**	**198**	**167**	**231**
Cs	**199**	**99**	**365**	**Bi**	**182**	**70**	**399**	**K**	**324**	**285**	**361**	**Tl**	**198**	**157**	**246**
Rb	**193**	**99**	**332**	**Cs**	**169**	**118**	**237**	**Rb**	**239**	**204**	**273**	**Ag**	**175**	**118**	**251**
S	**172**	**7**	**623**	**S**	**155**	**51**	**317**	**Ag**	**190**	**148**	**239**	**Rb**	**134**	**105**	**166**
As	*142*	*–3*	*551*	**W**	**148**	**60**	**283**	**Cs**	**163**	**131**	**199**	**Cs**	**109**	**71**	**156**
Sr	**94**	**37**	**193**	**Be**	**70**	**47**	**95**	**Ba**	**145**	**122**	**169**	**Na**	**88**	**75**	**103**
Bi	**75**	**6**	**202**	**Li**	**66**	**44**	**94**	**Be**	**80**	**67**	**94**	**Ba**	**88**	**61**	**120**
Mo	*64*	*–2*	*166*	*As*	*60*	*–7*	*179*	**Li**	**77**	**60**	**96**	**Li**	**61**	**39**	**85**
Na	**49**	**8**	**84**	**Mo**	**56**	**13**	**121**	**Na**	**67**	**55**	**79**	**Sr**	**54**	**36**	**77**
Be	*34*	*–12*	*93*	**Na**	**43**	**29**	**61**	**Mo**	**53**	**29**	**84**	**Be**	**47**	**33**	**62**
Pb	*18*	*–15*	*62*	**Cr**	**27**	**16**	**40**	**Cr**	**49**	**43**	**55**	*Se*	*9*	*–5*	*26*
Sn	*8*	*–11*	*31*	*Ag*	*22*	*–20*	*82*	**As**	**48**	**3**	**113**	*Ga*	*2*	*–3*	*7*
Li	*7*	*–16*	*35*	*Sr*	*13*	*–9*	*41*	**Sr**	**42**	**32**	**52**	*Ce*	*–1*	*–12*	*12*
Ga	*1*	*–13*	*19*	*Ni*	*4*	*–8*	*16*	**Se**	**21**	**10**	**33**	*La*	*–2*	*–12*	*10*
Ce	*0*	*–25*	*39*	*Sn*	*–2*	*–13*	*11*	**Ga**	**14**	**10**	**18**	*Cr*	*–2*	*–14*	*8*
U	*–2*	*–22*	*25*	*Ga*	*–6*	*–11*	*2*	**Ni**	**13**	**9**	**17**	*Mo*	*–3*	*–19*	*16*
La	*–3*	*–25*	*32*	*Se*	*–9*	*–20*	*4*	**Re**	**11**	**1**	**22**	*As*	*–5*	*–42*	*59*
Th	*–5*	*–27*	*25*	*Pb*	*–11*	*–24*	*5*	*Sn*	*5*	*–1*	*12*	*U*	*–8*	*–15*	*1*
Al	*–6*	*–20*	*11*	**Zn**	**–14**	**–24**	**–3**	*Cu*	*3*	*–10*	*17*	*Re*	*–9*	*–22*	*5*
V	*–8*	*–32*	*27*	*Ce*	*–15*	*–30*	*6*	*Cd*	*–2*	*–14*	*10*	*Cd*	*–9*	*–19*	*4*
Cr	*–9*	*–25*	*12*	*Re*	*–15*	*–29*	*2*	**Al**	**–6**	**–9**	**–3**	**Th**	**–10**	**–17**	**–1**
Re	*–11*	*–35*	*26*	*La*	*–17*	*–32*	*5*	**Co**	**–7**	**–10**	**–3**	**Sn**	**–10**	**–17**	**–2**
Se	*–14*	*–30*	*9*	**In**	**–18**	**–27**	**–10**	**V**	**–8**	**–13**	**–3**	**Al**	**–12**	**–15**	**–8**
Ti	*–17*	*–37*	*5*	**Ge**	**–18**	**–28**	**–6**	**U**	**–10**	**–16**	**–4**	**Pb**	**–13**	**–22**	**–2**
Ag	*–17*	*–47*	*27*	**U**	**–19**	**–34**	**–1**	**La**	**–10**	**–16**	**–3**	**Cu**	**–17**	**–29**	**–5**
In	*–17*	*–34*	*4*	**V**	**–20**	**–30**	**–10**	**Ce**	**–10**	**–16**	**–3**	**Ni**	**–18**	**–30**	**–10**
Ta	*–20*	*–36*	*3*	**Al**	**–21**	**–26**	**–14**	**Mg**	**–11**	**–15**	**–7**	**Ca**	**–21**	**–25**	**–18**
Nb	*–22*	*–41*	*2*	**Th**	**–24**	**–41**	**–7**	**Mn**	**–12**	**–15**	**–9**	**Zn**	**–23**	**–29**	**–15**
Ge	**–24**	**–40**	**–1**	**Co**	**–25**	**–32**	**–19**	**Zn**	**–12**	**–17**	**–5**	**Ti**	**–24**	**–27**	**–20**
Sc	**–25**	**–40**	**–4**	**Ti**	**–26**	**–34**	**–18**	**Sc**	**–12**	**–16**	**–7**	**Mn**	**–25**	**–28**	**–21**
Co	**–26**	**–35**	**–16**	**Nb**	**–28**	**–36**	**–19**	**In**	**–12**	**–17**	**–7**	**Nb**	**–25**	**–30**	**–19**
P	*–30*	*–50*	*3*	**P**	**–30**	**–49**	**–6**	**Fe**	**–13**	**–16**	**–11**	**Ta**	**–26**	**–31**	**–20**
Ni	**–31**	**–45**	**–16**	**Sc**	**–30**	**–38**	**–20**	**Ti**	**–13**	**–17**	**–10**	**Fe**	**–27**	**–30**	**–24**
Y	**–34**	**–47**	**–18**	**Ta**	**–31**	**–39**	**–21**	**Pb**	**–14**	**–21**	**–6**	**In**	**–28**	**–33**	**–21**
Fe	**–35**	**–44**	**–25**	**Mg**	**–32**	**–40**	**–25**	**Ca**	**–14**	**–18**	**–10**	**P**	**–30**	**–43**	**–15**
Sb	**–37**	**–54**	**–14**	**Mn**	**–32**	**–37**	**–26**	**Th**	**–15**	**–20**	**–9**	**Co**	**–30**	**–34**	**–26**
Cd	**–40**	**–58**	**–11**	**Cd**	**–32**	**–50**	**–10**	**Nb**	**–18**	**–22**	**–14**	**Mg**	**–30**	**–32**	**–27**
Zn	**–40**	**–52**	**–24**	**Fe**	**–32**	**–37**	**–27**	**Ge**	**–18**	**–24**	**–12**	**Ge**	**–34**	**–43**	**–23**
Mn	**–41**	**–52**	**–28**	**Ca**	**–41**	**–48**	**–35**	**Ta**	**–19**	**–23**	**–15**	**Y**	**–35**	**–38**	**–32**
Cu	**–42**	**–66**	**–2**	**Y**	**–42**	**–47**	**–37**	**Y**	**–27**	**–31**	**–23**	**Sc**	**–35**	**–39**	**–30**
Ca	**–43**	**–53**	**–33**	**Sb**	**–45**	**–58**	**–27**	**P**	**–44**	**–52**	**–34**	**V**	**–38**	**–43**	**–33**
Mg	**–45**	**–58**	**–31**	**Cu**	**–46**	**–59**	**–31**	**Sb**	**–52**	**–58**	**–45**	**Sb**	**–56**	**–63**	**–48**

using univariate concentration data (Eilu and Mikucki, 1996; Walshe et al., 2003), or relative mass change using ratios of univariate data (Prendergast, 2007). Univariate studies suffer from closure issues, ignoring apparent enrichment/depletion for elements of interest that relate to mobility of other elements. These studies also do not normalise values by rock type, and instead present ranges where upper and lower values are inferred to represent enrichment or depletion, respectively. While studies using element-ratios are not subject to problems related to either closure and normalisation to rock type, they can only present relative enrichment or depletion as unitless values. They also do not consider the heterogeneity of alteration domains or any statistical confidence for interpreted enrichment or depletion of key elements.

To illustrate that mass balance results provide new information, rather than rescaling raw compositional data, Fig. 12 shows P-P plots of original sample values versus computed mass change, per sample. Plotted points follow a linear trend, generally indicating that high values in raw data also indicate mass addition, and low raw values indicate mass loss. However, plotted samples are scattered, indicating a non-linear correlation between original concentration and calculated mass change. The P-P plot of K (Fig. 12) exhibits four separate trends, in order of increasing slope, for PB1–PB4. This relationship helps to illustrate an advantage to using rock-normalised mass balance results over compositionally-closed univariate data: calculated K addition is lower for PB1 on average than for PB4, considering identical K ppm values. The P-P plot for Na (Fig. 12) shows two trends for at least PB1 and PB3. This is interpreted to represent two distinct domains of Na mass change. P-P plots for Ca and Bi (Fig. 12) exhibit considerable overlap, suggesting similar mass balance domains present for both elements.

The total mass change is negative, given GMBE values < 1. Mass change estimates (PB1 = −23%; PB2 = −22%, PB3 = −1%; and PB4 = −10%) are inversely proportional to the magnitude of Au, S, and Te enrichment (Table 3). Table 4 gives element mass change estimates extracted from Table 3, for samples along the Au mineralisation-related albite-muscovite tie-line (Fig. 6). These values are selected because confidence limits do not span 0% mass change in any subunit, i.e., they are reliable average estimates. The elements associated with mafic rocks (group 1 from PCA; Fig. 8) include Ca, Co, Fe, Ge, Mg, Mn, and

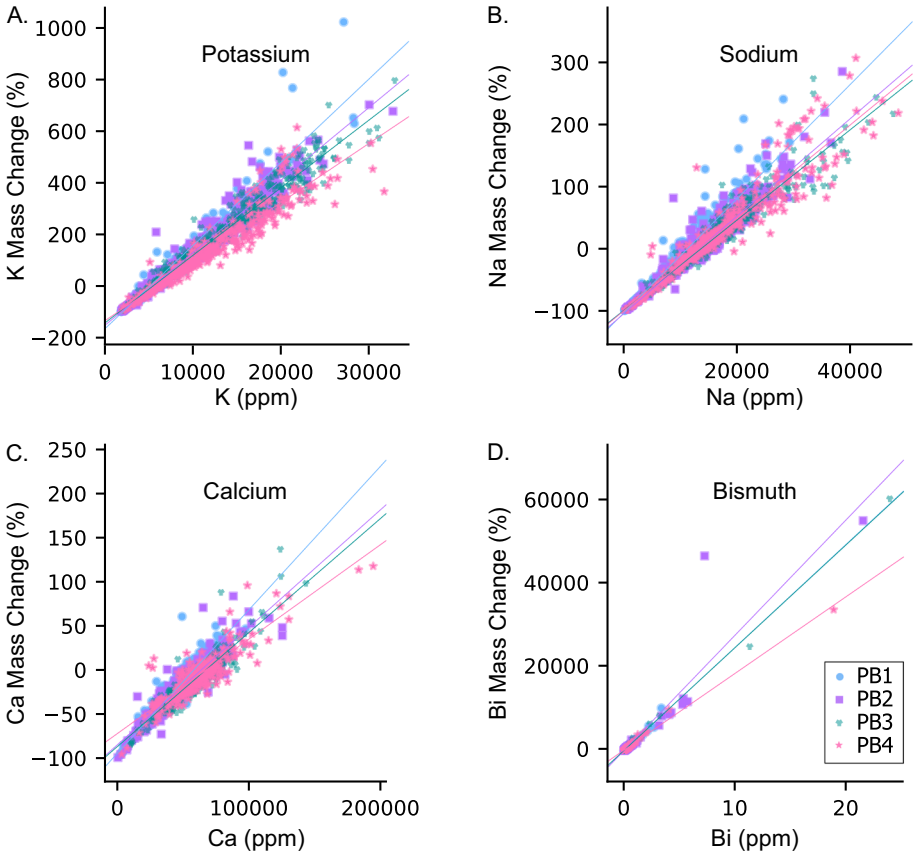

Fig. 12. Comparison of geochemical values: ppm vs. % mass change. A 1:1 linear relationship between original and derived data would signify perfect correlation between datasets. Points are plotted by Sample ID. Number of sample points per subunit are PB1: n = 433, PB2: n = 930, PB3: n = 931, and PB4: n = 432.

Zn, and are consistently depleted in the Au mineralised and altered rocks. The elements Sc and Y (group 2 from PCA; Fig. 8) provide erroneous results of depletion. This is interpreted as related to fractionation of the Paringa Basalt, as discussed above, and are not discussed further. The elements associated with potassic alteration are Ba, Cs, K, Rb, Tl (group 3 from PCA; Fig. 8) and are consistently enriched. Sodic alteration (group 4 from PCA; Fig. 8) is represented only by Na in Table 4, which is enriched. Confidence limits which span 0% for Sr (in PB2; Table 3) and Be (in PB1; Table 3) indicate these elements were omitted as they do not provide reliable average estimates in the sodic group. This effect is interpreted as related to heterogeneity of samples chosen to represent respective protolith sample suites and could possibly be resolved if new suites of protolith samples were selected.

The chalcophile elements (group 5 from PCA; Fig. 8) shown in Table 4 are Bi and W (enriched) and Sb (depleted). Finally, elements associated with Au mineralisation (group 5 from PCA; Fig. 8) are Au, S, and Te. These three elements are significantly enriched, although numerical estimates are erroneous as respective concentrations are below detection in protolith samples. The values are included mainly to represent noteworthy addition.

Orogenic Au literature describes the typical mineralisation-associated metasomatic enrichment of Tl, S, Ag, (± As, Sb, W, Te, Se, Mo, Bi, and B; McCuaig and Kerrich, 1998; Eilu and Groves, 2001). In general, this is consistent with Hamlet (Table 3), except in the case of As. The heterogeneity of As is high enough in all subdomains that reliable mass balance estimates cannot be produced, i.e., estimates have high associated uncertainty (Fig. 11). We note that while our low calculated depletion of Sb is not typical for orogenic deposit alteration zones, decoupling between Bi and Sb is described for the nearby Athena deposit (Walshe et al., 2014). Arsenic and Sb enrichment zones in orogenic Au deposits are have been associated with pyrite – pyrrhotite alteration mineral assemblages (reduced), whereas Bi and Mo enrichment zones are associated with an assemblage of pyrite – magnetite (oxidised; Neumayr et al., 2008). Pyrite and pyrrhotite are two hallmark sulphides in the Au mineralised Hamlet Shear Zone (Fig. 3), while magnetite is rare (Walshe et al., 2003; Walshe et al., 2014). We therefore interpret the observed alteration mineral phases, in conjunction with Sb depletion and Bi addition, to indicate a reduced Au mineralisation event at Hamlet.

6.4. Permeability networks from mass balance estimates

Mass balance trends for key elements K, Na, Ca, and Bi are presented on long sections in Fig. 13. Potassium and Na are typically associated with minerals which are spatially coincident with orogenic Au mineralisation (Groves, 1993). Sodium and K are broadly enriched at Hamlet (Fig. 11; Table 4). Metasomatism during the development of orogenic shear zones has been shown to involve the hydrolysis of feldspar (McCuaig and Kerrich, 1998), interpreted to be expressed at Hamlet as the potassic group (additions of K, Rb, Ba, Cs and Tl) and sodic group (addition of Na). Respectively this corresponds to pervasive biotite developed as an envelope within the shear zone, and to albite associated with local pervasive alteration, veining, and breccia infill.

There are numerous associations between Na, K, and Au-bearing fluids in orogenic Au deposits, including mafic-hosted examples in the Yilgarn (Ames et al., 1991; Eilu and Mikucki, 1996; Groves et al., 1998; McCuaig and Kerrich, 1998; Nguyen et al., 1998; Knight et al., 2000; Eilu and Groves, 2001). The presence of biotite is important, as fluid-driven mica formation promotes ductile deformation and permeability enhancement of Au-hosting shear zones (Dipple and Ferry, 1992). The regions interpreted to represent enhanced ductile deformation zones are given by enrichment shown in Fig. 13A.

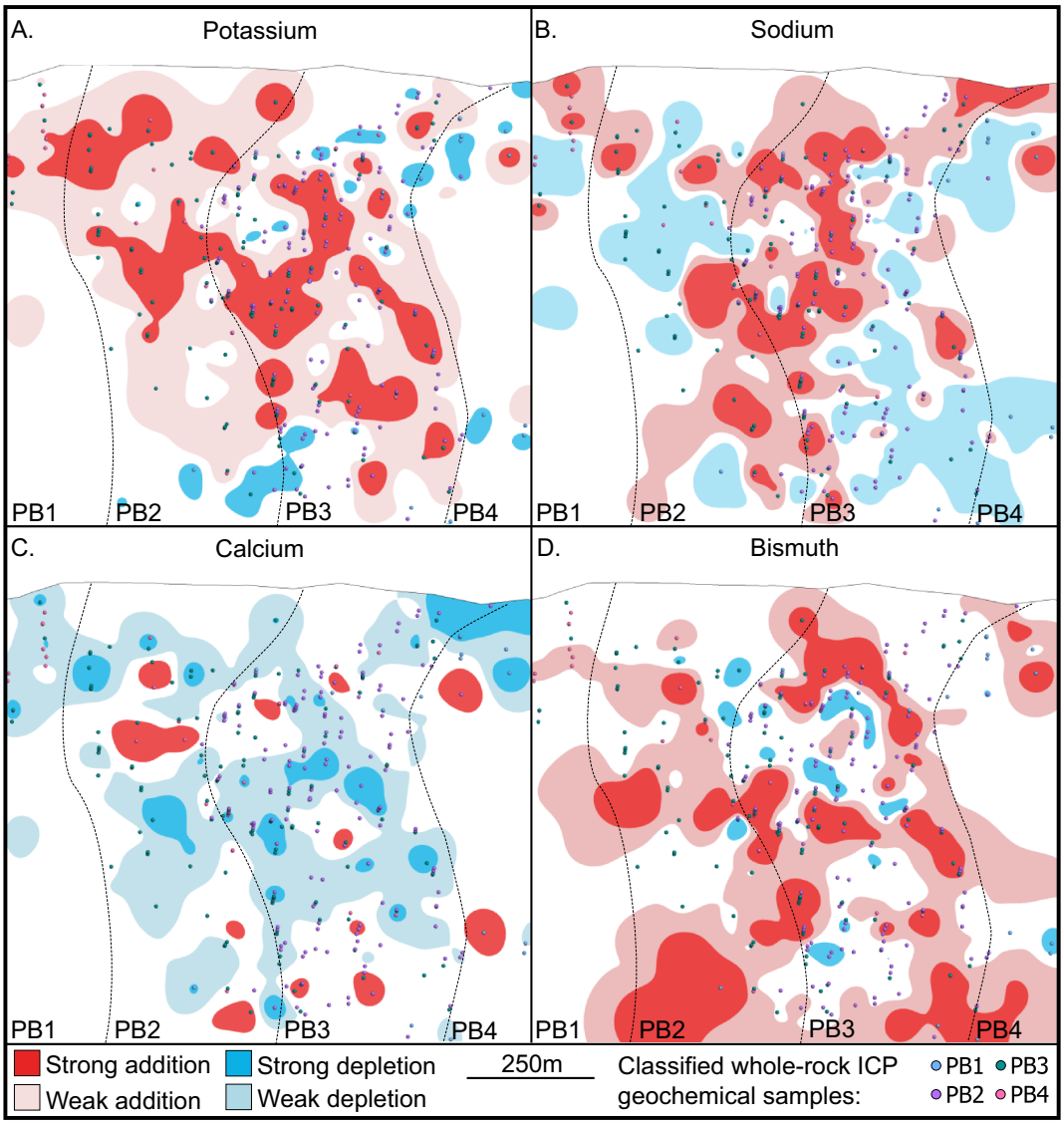

Fig. 13. Long-sections of the Hamlet shear, looking west. The section is inclined, dipping 32° towards 279°, to best orient the Hamlet shear plane parallel to the page. Clipping is ± 25 m about the section plane. Mass balance contours are projected to that plane. Approximate upper and lower quartiles of mass balance values used to represent 'strong' enrichment or depletion, respectively; cut off thresholds and interpolation parameters are given in Appendix D. Interpolation Parameters. Subunit boundaries are shown as dashed lines.

Given that albite veining and breccia zones are observed to overprint biotite-altered Paringa Basalt (Fig. 3), we interpret sodic alteration (i.e., Na enrichment; Fig. 13B) to overprint potassic alteration (i.e., K enrichment; Fig. 13A). This important relationship represents the facilitation of failure mode transition from ductile to brittle failure, with consequent implications for the nature of fluid flow paths. Albite thus provides a mineralogical control on fault-valve style mineralisation, which has been previously described for other Au deposits in the St Ives camp (Sibson, 1987; Nguyen et al., 1998; Cox, 2005). The pathway of albitisation is interpreted as coincident with Na-enrichment zones (Fig. 13B).

Calcium represents a major mafic-associated element, related to plagioclase in protolith rocks, which is consistently depleted across all subunits. Because Ca is a likely substituted for by K or Na during alteration, we interpret the pattern shown in Fig. 13C to be the inverse of potassic and sodium enrichments. Mapping Ca is thus less useful for understanding pathways of unique metasomatic changes, but potentially represents a general fluid flow network.

Finally, Bi (Fig. 13D) is included as a chalcophile element described in the literature as forming a halo around many orogenic Au deposits (Groves, 1993). Geochemically, Bi is the closest chalcophile element to Au, S, and Te in PC space at Hamlet (Fig. 8). This relationship compliments literature which describes Bi as occurring in bismuth-tellurides associated with Au (Ciobanu et al., 2005; Goldfarb et al., 2005; Tooth et al., 2011).

6.5. *Mass balance models as a proxy for Au mineralisation*

Fig. 14 presents mass balance data for Bi in 3-D. While contoured regions are used to interpret spatial continuity orientations of Bi mass balance in Fig. 13D, individual points are used in Fig. 14 to provide an interpretation of possible fluid flow network segments. The trend-plunge of segments are constrained by geostatistical interpolation around Bi enrichment (parameters are given in Appendix D. Interpolation Parameters). These interpolated wireframes of Bi addition are coincident with zones of Au mineralisation given by block model estimation (Fig. 14).

Four trends of Bi addition are interpreted using strongest Bi addition: steeply dipping plunges to the northeast and south-southeast, and shallowly dipping plunges to the north-northeast and southeast

Table 4
Mass balance estimates for elements where confidence limits do not span 0%. Samples are from Au mineralised and altered domains of the Hamlet orebody, across the four Paringa Basalt subunits (PB1–PB4). Data are extracted from Table 3. Labels (1. Mafic; 2. Immobile; 3. Potassic; 4. Sodic; 5. Chalcophile; and 6. Gold) relate to covariance of elements indicated by PCA (Fig. 8). Immobile element results (in italics) are erroneous and interpreted as related to fractionation of the Paringa Basalt. Gold results (also in italics) are erroneous and extremely high because the concentration of this element in protolith samples is below detection.

			PB1 Mass Bal. (%)	PB2 Mass Bal. (%)	PB3 Mass Bal. (%)	PB4 Mass Bal. (%)
Mafic	1	Ca	–43	–41	–14	–21
		Co	–26	–25	–7	–30
		Fe	–35	–32	–13	–27
		Ge	–24	–18	–18	–34
		Mg	–45	–32	–11	–30
		Mn	–41	–32	–12	–25
		Zn	–40	–14	–12	–23
Immobile	2	*Sc*	*–25*	*–30*	*–12*	*–35*
		Y	*–34*	*–42*	*–27*	*–35*
Potassic	3	Ba	227	203	145	88
		Cs	199	169	163	109
		K	269	235	324	198
		Rb	193	195	239	134
		Tl	237	314	327	198
Sodic	4	Na	49	43	67	88
Chalcoph.	5	Bi	75	182	379	302
		Sb	–37	–45	–52	–56
		W	230	148	498	330
Gold	6	*Au*	*3352*	*3704*	*138962*	*61418*
		S	*172*	*155*	*516*	*479*
		Te	*255*	*664*	*1298*	*944*

(Fig. 14). The geometry of these trends suggests the type of spatial repetition that might be present as a fluid flow mesh across the shear zone, similar to that described as occurring orogenic shear systems (Sibson, 1996; Cox, 2005).

Mass balance models provide normalised evidence for geochemical continuity across a shear zone. In the case of Bi (Figs. 13D and 14), enrichment zones may represent a separate, complimentary dataset to that of Au from fire assay, i.e., what is used for conventional variography and block modeling. Because geochemical data has a lower mathematical nugget (i.e., values are more consistent along trends, Hill et al., 2014a, 2014c, 2014b), other elements may be more effective at mapping the distribution of the mineralisation than Au itself. At minimum, Bi mass balance results at Hamlet provide a practical independent dataset to corroborate Au trends.

7. Conclusions

Our study improves the geochemical understanding of element mobility in shear-associated, greenstone-hosted orogenic Au deposits by presenting statistically-robust mass balance estimates for the Au-mineralised Hamlet Shear Zone, using a method that addresses the compositional heterogeneity of protolith and altered rocks. Principal components analysis is first used to show covarying elements and six groups of elements are identified: (1) relatively immobile elements: Zr and Hf provide the appropriate reference frame for mass balance calculations; (2) elements associated with mafic rocks, like Ca, Fe, Mg, and Cr; (3) elements related to potassic alteration: Ba, Cs, K, Rb, and Tl enrichment; (4) elements related to sodic alteration: Be, Na, and Sr enrichment; (5) chalcophile elements, including Bi and Sb; and (6) Au, Te, and S representing Au-mineralisation.

Mass balance confidence limits of 95% are used to discriminate

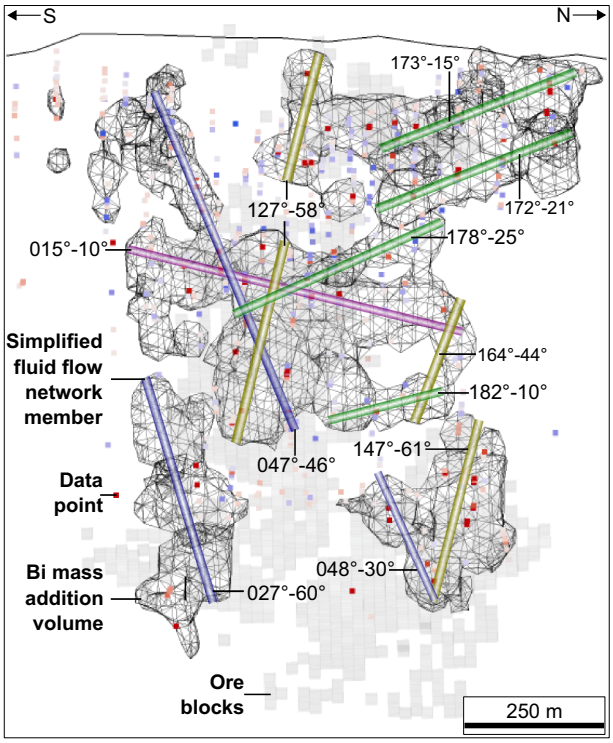

Fig. 14. A constrained geometric interpretation for Bi mass balance results. The inclined long section dips 32° towards 279°, approximately co-planar to the Hamlet shear. Clipping is ± 50 m across the long-section plane. Bismuth mass addition trends are given, based on wireframes interpolated around the highest mass balance values (see Appendix D. Interpolation Parameters) and the visual assessment of linear continuity using 3-D plots (after Cowan, 2014) for mass addition > 80%. Apparent trends include steeply plunging orientations to the north (blue) and south (yellow), and gently plunging orientations towards the north (purple) and south (green). Estimated average lineations are labelled as trend-plunge. Ore blocks (light grey) are filtered to ≥1 g/t, and clipped to the section plane, to provide an indication of mineralisation geometry from fire assay data. Coloured data points represent Bi mass balance results calculated from whole rock geochemical assays. (For interpretation of the references to colour in this figure legend, the reader is referred to the web version of this article.)

elements with estimates that differ from zero at a statistically significant level, i.e., with mass changes above a minimum detectable amount. Mass balance estimates associated with Au mineralisation across four subunits of Paringa Basalt are similar, with up to 24% total rock mass loss. Estimates for the statistically-reliable potassic and sodic group elements indicate enrichment in the mineralised zones, likely at the expense of elements with a mafic-association. The decoupling of Bi (enriched) and Sb (depleted), along with observed pyrite and pyrrhotite in mineralised rocks, is consistent with Au mineralisation by a reduced fluid. These results are comparable to other Archaean greenstone-hosted Au deposits of the Yilgarn.

Using K, Na, Ca, and Bi, spatial mass balance models are made for the Hamlet Shear Zone and the resulting geometry is suggestive of fluid-flow zones with conjugate pathways. Potassium enrichment is interpreted to represent zones of biotite development, and Na to represent albitisation. Calcium depletion best represents overall fluid pathways (feldspar-destructive alteration), and Bi addition provides a spatial proxy for Au mineralisation (likely Bi-tellurides). Considered as network members represented in 3-D, results provide a valuable geochemical representation of metasomatism associated with fluid-focusing structures in an orogenic Au deposit and corroborate the roles of K (for biotite-related strain softening) and Na (for albite-related failure-mode transition) and support the orogenic Au fault-valve

mineralisation model.

Supplementary data to this article can be found online at https://doi.org/10.1016/j.chemgeo.2019.03.022.

Acknowledgements

We wish to thank Gold Fields Australasia Ltd. for providing data for this study, and especially to Heidi Pass for her time and assistance facilitating the project. Discussions with Sarah Jones (Chief Structural Geologist for Gold Fields Australasia Ltd.) were very valuable to ensure our results conformed to the current structural understanding of the Hamlet Deposit. The authors would like to thank Jay Ague for supplying the original Fortran code and study data presented in Ague and van Haren (1996); these were fundamental to recreating their method in Python and validating our implementation. Ayesha Ahmed provided insightful discussion and comments that greatly improved the paper. We sincerely thank Stephen Cox, Nico Thebaud, and Anonymous Reviewer #1 for their time and highly valuable reviews, when the paper was initially submitted to the *Journal of Precambrian Research* and suggested for transfer (June 2018). The final version of this paper was enhanced by reviewer Carl Brauhart and Anonymous Reviewer #2; we appreciate their time and effort. We also appreciate assistance from Ron Berry to reduce the final length of the paper. This research was funded by the Australian Research Council Research Hub for Transforming the Mining Value Chain (project number IH130200004).

References

Ague, J.J., van Haren, J.L.M., 1996. Assessing metasomatic mass and volume changes using the bootstrap, with application to deep crustal hydrothermal alteration of marble. Econ. Geol. Bull. Soc. Econ. Geol. 91, 1169–1182.
Ahmed, A.D., Hood, S.B., Gazley, M.F., Cooke, D.R., Orovan, E.A., 2019. Interpreting element addition and depletion at the Ann Mason porphyry-Cu deposit, Nevada, using mapped mass balance patterns. J. Geochem. Explor. 196, 81–94.
Aitchison, J., 1986. The Statistical Analysis of Compositional Data: London. 416 Chapman and Hall.
Aitchison, J., 1989. Measures of Location of Compositional Data Sets. Math. Geol. 21, 787–790.
Aitchison, J., 2008. The single principle of compositional data analysis, continuing fallacies, confusions and misunderstandings and some suggested remedies, CODAWORK'08: 3rd Compositional Data Analysis Workshop: Girona.
Ames, D.E., Franklin, J.M., Froese, E., 1991. Zonation of hydrothermal alteration at the San Antonio gold mine, Bissett, Manitoba, Canada. Econ. Geol. 86, 600–619.
Barnes, S.J., Van Kranendonk, M.J., Sonntag, I., 2012. Geochemistry and tectonic setting of basalts from the Eastern Goldfields Superterrane. Aust. J. Earth Sci. 59, 707–735.
Baumgartner, L.P., Olsen, S.N., 1995. A least-squares approach to mass-transport calculations using the isocon method. Econ. Geol. Bull. Soc. Econ. Geol. 90, 1261–1270.
Blewett, R.S., Squire, R., Miller, J.M., Henson, P.A., Champion, D.C., 2010. Architecture and geodynamic evolution of the St Ives Goldfield, eastern Yilgarn Craton, Western Australia. Precambrian Res. 183, 275–291.
Brauhart, C.W., Grunsky, E.C., Hagemann, S.G., 2017. Magmato-hydrothermal space: a new metric for geochemical characterisation of metallic ore deposits. Ore Geol. Rev. 86, 867–895.
Brimhall, G.H., Dietrich, W.E., 1987. Constitutive mass balance relations between chemical composition, volume, density, porosity, and strain in metasomatic hydrochemical systems: results on weathering and pedogenesis. Geochim. Cosmochim. Acta 51, 567–587.
Brimhall, G.H., Lewis, C.J., Ague, J.J., Dietrich, W.E., Hampel, J., Teague, T., Rix, P., 1988. Metal enrichment in bauxites by deposition of chemically mature aeolian dust. Nature 333, 819–824.
Caciagli, N., 2015. Multielement Geochemical Modelling for Mine Planning: Case Study From an Epithermal Gold Deposit: International Workshop on Compositional Data Analysis, 2015, p. pp. 45–61.
Cann, J.R., 1970. Rb, Sr, Y, Zr and Nb in some ocean floor basaltic rocks. Earth Planet. Sci. Lett. 10, 7–11.
Carolus, C., 2018, Gold Fields 2017 Integrated Annual Report; Mineral Resources and Mineral Reserves Supplement: Johannesburg, p. 144.
Carranza, E.J.M., 2011. Analysis and mapping of geochemical anomalies using logratio-transformed stream sediment data with censored values. J. Geochem. Explor. 110, 167–185.
Carranza, E.J.M., 2017. Geochemical mineral exploration: should we use enrichment factors or log-ratios? Nat. Resour. Res. 26, 411–428.
Carrasco, T., Girty, G., 2015. Identifying a reference frame for calculating mass change during weathering: a review and case study utilizing the C# program assessing element immobility and critical ratio methodology. Catena 125, 146–161.
Chandrajith, R., Dissanayake, C., Tobschall, H., 2001. Application of multi-element relationships in stream sediments to mineral exploration: a case study of Walawe Ganga Basin, Sri Lanka. Appl. Geochem. 16, 339–350.
Ciobanu, C.L., Cook, N.J., Pring, A., 2005. Bismuth Tellurides as Gold Scavengers: Mineral Deposit Research: Meeting the Global Challenge, 2005, p. pp. 1383–1386.
Connors, K., Donaldson, J., Morrison, B., Davy's, C., and Neumayr, P., 2005, The Stratigraphy of the Kambalda-St Ives district: Workshop notes: Kambalda, St Ives Gold Mine, Gold Fields Pty. Ltd.
Cowan, E., 2014. X-ray Plunge Projection: Understanding Structural Geology from Grade Data. AusIMM Monograph, v. 30. pp. 207–220.
Cox, S., 2005. Coupling between deformation, fluid pressures, and fluid flow in ore-producing hydrothermal systems at depth in the crust: Economic Geology. 100. Bulletin of the Society of Economic Geologists, pp. 39–75.
Cox, S.F., Ruming, K., 2004. The St Ives mesothermal gold system, Western Australia—a case of golden aftershocks? J. Struct. Geol. 26, 1109–1125.
Czarnota, K., Champion, D.C., Goscombe, B., Blewett, R.S., Cassidy, K.F., Henson, P.A., Groenewald, P.B., 2010. Geodynamics of the eastern Yilgarn Craton. Precambrian Res. 183, 175–202.
Davies, J., Whitehead, R., 2006. Alkali-alumina and MgO-alumina molar ratios of altered and unaltered rhyolites. Explor. Min. Geol. 15, 75–88.
Davies, J., Whitehead, R., 2010. Alkali/alumina molar ratio trends in altered granitoid rocks hosting porphyry and related deposits. Explor. Min. Geol. 19, 13–22.
de Caritat, P., Grunsky, E.C., 2013. Defining element associations and inferring geological processes from total element concentrations in Australian catchment outlet sediments: Multivariate analysis of continental-scale geochemical data. Appl. Geochem. 33, 104–126.
Dipple, G.M., Ferry, J.M., 1992. Metasomatism and fluid flow in ductile fault zones. Contrib. Mineral. Petrol. 112, 149–164.
Efron, B., 1979. Bootstrap methods: another look at the jackknife. Ann. Stat. 7, 1–26.
Eilu, P., Groves, D., 2001. Primary alteration and geochemical dispersion haloes of Archaean orogenic gold deposits in the Yilgarn Craton: the pre-weathering scenario. Geochem. Explor. Environ. Anal. 1, 183–200.
Eilu, P., Mikucki, E., 1996. Geochemical and isotopic dispersion haloes in Archean lode-gold systems: assessment of alteration indices for use in district-scale and mine-scale exploration. In: Minerals and Energy Research Institute of Western Australia Report. vol. 176.
Fisher, L., Gazley, M.F., Baensch, A., Barnes, S.J., Cleverley, J., Duclaux, G., 2014. Resolution of geochemical and lithostratigraphic complexity: a workflow for application of portable X-ray fluorescence to mineral exploration. Geochem. Explor. Environ. Anal. 2012–2158.
Floyd, P., Winchester, J., 1978. Identification and discrimination of altered and metamorphosed volcanic rocks using immobile elements. Chem. Geol. 21, 291–306.
Gazley, M.F., Collins, K.S., Roberston, J., Hines, B.R., Fisher, L.A., McFarlane, A., 2015. Application of principal component analysis and cluster analysis to mineral exploration and mine geology. In: AusIMM New Zealand Branch Annual Conference. 2015. Dunedin, New Zealand, pp. 131–139.
Goldfarb, R.J., Baker, T., Dube, B., Groves, D.I., Hart, C.J., Gosselin, P., 2005. Distribution, Character, and Genesis of Gold Deposits in Metamorphic Terranes: Economic Geology 100th Anniversary Volume. pp. 40.
Grant, J.A., 1986. The isocon diagram — a simple solution to Gresens equation for metasomatic alteration. Econ. Geol. 81, 1976–1982.
Grant, J.A., 2005. Isocon analysis: a brief review of the method and applications. Phys. Chem. Earth 30, 997–1004.
Gregory, D.D., Large, R.R., Bath, A.B., Steadman, J.A., Wu, S., Danyushevsky, L., Bull, S.W., Holden, P., Ireland, T.R., 2016. Trace element content of pyrite from the Kapai Slate, St. Ives Gold District, Western Australia. Econ. Geol. 111, 1297–1320.
Gresens, R.L., 1967. Composition-volume relationships of metasomatism. Chem. Geol. 2, 47–65.
Groves, D., 1993. The crustal continuum model for late-Archaean lode-gold deposits of the Yilgarn Block, Western Australia. Mineral. Deposita 28, 366–374.
Groves, D.I., Goldfarb, R.J., Gebre-Mariam, M., Hagemann, S.G., Robert, F., 1998. Orogenic gold deposits: a proposed classification in the context of their crustal distribution and relationship to other gold deposit types. Ore Geol. Rev. 13, 7–27.
Grunsky, E.C., Smee, B.W., 1999. The differentiation of soil types and mineralization from multi-element geochemistry using multivariate methods and digital topography. J. Geochem. Explor. 67, 287–299.
Grunsky, E.C., Mueller, U.A., Corrigan, D., 2014. A study of the lake sediment geochemistry of the Melville Peninsula using multivariate methods: applications for predictive geological mapping. J. Geochem. Explor. 141, 15–41 v.
Hill, E.J., Oliver, N.H., Cleverley, J., Nugus, M., 2014a. Modelling ore bodies of high-nugget gold using conditional probability. In: Mathematics of Planet Earth. Springer, pp. 5–8.
Hill, E.J., Oliver, N.H., Fisher, L., Cleverley, J.S., Nugus, M.J., 2014b. Using geochemical proxies to model nuggety gold deposits: an example from Sunrise Dam, Western Australia. J. Geochem. Explor. 145, 12–24.
Hill, E.J., Oliver, N.H., Cleverley, J.S., Nugus, M.J., Carswell, J., Clark, F., 2014c. Characterisation and 3D modelling of a nuggety, vein-hosted gold ore body, Sunrise Dam, Western Australia. J. Struct. Geol. 67, 222–234.
Janousek, V., Farrow, C.M., Erban, V., 2006. Interpretation of whole-rock geochemical data in igneous geochemistry: introducing Geochemical Data Toolkit (GCDkit). J. Petrol. 47, 1255–1259.
Jenner, G.A., 1996. Trace Element Geochemistry of Igneous Rocks: Geochemical Nomenclature and Analytical Geochemistry: Trace Element Geochemistry of Volcanic Rocks: Applications for Massive Sulfide Exploration. pp. 51–77.
Jolliffe, I., 2011. Principal Component Analysis. Springer.
Knight, J.T., Ridley, J.R., Groves, D.I., 2000. The Archean amphibolite facies Coolgardie goldfield, Yilgarn craton, Western Australia: nature, controls, and gold field-scale patterns of hydrothermal wall-rock alteration. Econ. Geol. 95, 49–84.

Krapež, B., Hand, J.L., 2008. Late Archaean deep-marine volcaniclastic sedimentation in an arc-related basin: the Kalgoorlie Sequence of the Eastern Goldfields Superterrane, Yilgarn Craton, Western Australia. Precambrian Res. 161, 89–113.
Lesher, C.M., 1983. Localization and Genesis of Komatiite-associated Fe-Ni-Cu Sulphide Mineralization at Kambalda, Western Australia. In: University of Western Australia.
Lopez-Moro, F.J., 2012. EASYGRESGRANT-A Microsoft Excel spreadsheet to quantify volume changes and to perform mass-balance modeling in metasomatic systems. Comput. Geosci. 39, 191–196.
Loughlin, W., 1991. Principal component analysis for alteration mapping: Photogrammetric Engineering and Remote Sensing. 57. pp. 1163–1169.
MacLean, W., 1990. Mass change calculations in altered rock series. Mineral. Deposita 25, 44–49.
McCuaig, T.C., Kerrich, R., 1998. P-T-t-deformation-fluid characteristics of lode gold deposits: evidence from alteration systematics: Ore Geology Reviews. 12. pp. 381–453.
McGoldrick, K., Squire, R.J., Cas, R., Briggs, M., Tunjic, J., Allen, C.M., Campbell, I., Hayman, P., 2013a. The largest Au deposits in the St Ives Goldfield (Yilgarn Craton, Western Australia) may be located in a major Neoarchean volcano-sedimentary depocentre. Mineral. Deposita 48, 861–881.
McGoldrick, K.L., Squire, R.J., Cas, R.A.F., Briggs, M., Tunjic, J., Allen, C.M., Campbell, I.H., Hayman, P.C., 2013b. The largest Au deposits in the St Ives Goldfield (Yilgarn Craton, Western Australia) may be located in a major Neoarchean volcano-sedimentary depo-centre. Mineral. Deposita 48, 861–881.
McKinley, J.M., Hron, K., Grunsky, E.C., Reimann, C., de Caritat, P., Filzmoser, P., van den Boogaart, K.G., Tolosana-Delgado, R., 2016. The single component geochemical map: fact or fiction? J. Geochem. Explor. 162, 16–28.
Miller, J., Blewett, R., Tunjic, J., Connors, K., 2010. The role of early formed structures on the development of the world class St Ives Goldfield, Yilgarn, WA. Precambrian Res. 183, 292–315.
Mukherjee, P.K., Gupta, P.K., 2008. Arbitrary scaling in ISOCON method of geochemical mass balance: an evaluation of the graphical approach. Geochem. J. 42, 247–253.
Myers, J.S., 1997. Preface: Archaean geology of the eastern goldfields of Western Australia - regional overview. Precambrian Res. 83, 1–10.
Nesbitt, H., Young, G., 1984. Prediction of some weathering trends of plutonic and volcanic rocks based on thermodynamic and kinetic considerations. Geochim. Cosmochim. Acta 48, 1523–1534.
Neumayr, P., Walshe, J.L., Hagemann, S.G., Petersen, K., Roache, R., Frikken, P., Horn, L., Halley, S., 2008. Oxidized and reduced mineral assemblages in greenstone belt rocks of the St. Ives gold camp, Western Australia: vectors to high-grade ore bodies in Archaean gold deposits? Mineral. Deposita 43, 363–371.
Nguyen, P.T., Cox, S.F., Harris, L.B., Powell, C.M., 1998. Fault-valve behaviour in optimally oriented shear zones: an example at the Revenge gold mine, Kambalda, Western Australia. J. Struct. Geol. 20, 1625–1640.
Ohta, T., Arai, H., 2007. Statistical empirical index of chemical weathering in igneous rocks: a new tool for evaluating the degree of weathering. Chem. Geol. 240, 280–297.
Pawlowsky-Glahn, V., Egozcue, J.J., Tolosana-Delgado, R., 2015. Modeling and Analysis of Compositional Data. John Wiley & Sons.
Pearce, J.A., 1996. A user's Guide to Basalt Discrimination Diagrams: Trace Element Geochemistry of Volcanic Rocks: Applications for Massive Sulphide Exploration. Geological Association of Canada, Short Course Notes. 12. pp. 113.
Pearce, J.A., Cann, J.R., 1973. Tectonic setting of basic volcanic rocks determined using trace element analyses. Earth Planet. Sci. Lett. 290–300.
Pearson, K., 1901. LIII. On lines and planes of closest fit to systems of points in space. Lond. Edinb. Dublin Philos. Mag. J. Sci. 2, 559–572.
Piercey, S.J., Mortensen, J.K., Murphy, D.C., Paradis, S., Creaser, R.A., 2002. Geochemistry and tectonic significance of alkalic mafic magmatism in the Yukon-Tanana terrane, Finlayson Lake region, Yukon. Can. J. Earth Sci. 39, 1729–1744.
Potdevin, J.L., 1993. Gresens-92 - a simple Macintosh program of the Gresens method. Comput. Geosci. 19, 1229–1238.
Prendergast, K., 2007. Application of lithogeochemistry to gold exploration in the St Ives goldfield, Western Australia. Geochem. Explor. Environ. Anal. 7, 99–108.
Reimann, C., 2005. Geochemical mapping: technique or art? Geochem. Explor. Environ. Anal. 5, 359–370.
Reimann, C., Filzmoser, P., 2000. Normal and lognormal data distribution in geochemistry: death of a myth. Consequences for the statistical treatment of geochemical and environmental data. Environ. Geol. 39, 1001–1014.
Rollinson, H.R., 2014. Using geochemical data: evaluation, presentation, interpretation. Routledge.
Ruming, K. J., 2006, Controls on Lode Gold Mineralisation in the Victory Thrust Complex, St Ives Goldfield, Western Australia, University of Newcastle.
Sibson, R.H., 1987. Earthquake Rupturing as a Mineralizing Agent in Hydrothermal Systems. Geology 15, 701–704.
Sibson, R.H., 1996. Structural permeability of fluid-driven fault-fracture meshes. J. Struct. Geol. 18, 1031–1042.
Spiegel, M.R., 1961. Theory and Problems of Statistics. McGraw-Hill, NY ISBN 10: 0070602271, ISBN 13: 9780070602274.
Squire, R.J., Cas, R.A.F., Clout, J.M.F., Behets, R., 1998. Volcanology of the Archaean Lunnon Basalt and its relevance to nickel sulfide-bearing trough structures at Kambalda, Western Australia. Aust. J. Earth Sci. 45, 695–715.
Stanley, C., Madeisky, H., 1996. Lithogeochemical Exploration for Metasomatic Zones Associated with Hydrothermal Mineral Deposits Using Pearce Element Ratio Analysis: Short Course Notes on Pearce Element Ratio Analysis.
Swager, C.P., Griffin, T.J., Witt, W.K., Wyche, S., Ahmat, A.L., Hunter, W.M., McGoldrick, P.J., 1995. Geology of the Archaean Kalgoorlie Terrane — an Explanatory Note. pp. 26.
Tooth, B., Ciobanu, C.L., Green, L., O'Neill, B., Brugger, J., 2011. Bi-melt formation and gold scavenging from hydrothermal fluids: an experimental study. Geochim. Cosmochim. Acta 75, 5423–5443.
Urqueta, E., Kyser, T.K., Clark, A.H., Stanley, C.R., Oates, C.J., 2009. Lithogeochemistry of the Collahuasi porphyry Cu–Mo and epithermal Cu–Ag (–Au) cluster, northern Chile: Pearce element ratio vectors to ore. Geochem. Explor. Environ. Anal. 9, 9–17.
Vistelius, A.B., 1960. The Skew Frequency Distributions and the Fundamental Law of the Geochemical Processes. J. Geol. 68, 1–22 v.
Walshe, J., Halley, S., Hall, G., Kitto, P., 2003. Contrasting fluid systems, chemical gradients and controls on large-tonnage, high-grade Au deposits, Eastern Goldfields Province, Yilgarn Craton, Western Australia, Mineral Exploration and Sustainable Development. pp. 827–830.
Walshe, J.L., Bath, A.B., Cloutier, J., Hough, M.A., 2014. High grade Au deposits: processes to prediction, MERIWA 410 final report. In: Geological Survey of Western Australia Report. 145. pp. 183.
Whitbread, M.A., McQueen, K.G., 2002. Ratio Analysis of Bulk Geochemical Data: Tracking Ore-related Cryptic Alteration by Modelling Mineral Changes: Regolith and Landscapes in Eastern Australia. pp. 133–135.
Wood, D.A., 1980. The application of a ThHfTa diagram to problems of tectonomagmatic classification and to establishing the nature of crustal contamination of basaltic lavas of the British Tertiary Volcanic Province. Earth Planet. Sci. Lett. 50, 11–30.
Woronow, A., Love, K.M., 1990. Quantifying and testing differences among means of compositional data suites. Math. Geol. 22, 837–852.